Hydrogen Bonding, Electron Transfer and Orbital Interactions between RDX and Al₃O₃⁻ : Forces governing the initial encounter

Fatma Ahu AKIN

Boğaziçi University, Department of Chemistry, Bebek, Istanbul/Turkey

ahu.akin@boun.edu.tr

ABSTRACT

As the first step in energy transfer from oxide passivated metal nanoparticles/surface defects to an energetic molecule for the controlled dissociation of the latter, the nature of the weak interactions between RDX and $Al_3O_3^-$ isomers are studied as a model system by DFT method with PBE0 functional and different basis sets (TZVP, Def2-TZVPP, TZ2P). Different electron density (NCI, IGMH, QTAIM, IQA, EDA-NOCV) and charge analysis methods (Hirshfeld, Mulliken, Hirshfeld-I, NPA) reveal that partial charge-transfer from $Al_3O_3^-$ to RDX via the C-H···O (1.851-2.481Å, O(2p)-to-C-H(σ*) type) and the C-H···Al (2.836-2.871Å, Al(3p)-to-C-H(σ*) type) interactions are possible. Hirshfeld analysis predicts 6-25% transfer of the -1 charge to RDX while Hirshfeld-I, NPA, and Mulliken predict 7-22%, 2-7%, and 7-13% transfer, respectively. $Al_3O_3^-$ (HOMO)-RDX (LUMO+n, n=0-3) type interactions including the charge transfer via the (ON)O···Al (2.846-3.511Å) interactions are found to excite the $Al_3O_3^-$ (kite) anion. The binding energies are in the -10 to -31 kcal/mol range. Vertical detachment energies of the complexes are within 2.5-3.9 eV, higher than the bare $Al_3O_3^-$ isomers by 0.3-1.3 eV. Complexation weakens the RDX structure and reduces the C-H stretching frequencies by 10-350 cm⁻¹. Modulations in the bond lengths in the $Al_3O_3^-$ isomers shift the frequencies in the 0-1300 cm⁻¹ region. New intermolecular vibrations enrich the terahertz region of the IR spectra. Complexation is found to augment the resultant dipole moment from 2.7 ($Al_3O_3^-$ (*rec*)) and 8.6 ($Al_3O_3^-$ (*kite*)) to the 2.9-16.0 Debye range, signalling effects on the workfunction of the aluminum oxide surfaces upon binding.

Keywords: RDX, aluminum oxide, cluster, DFT, anion, electron transfer, surface defects

Introduction:

Nanoenergetic solid propellant design, explosives detection, and nitroaromatics degradation at metal oxide surfaces are all concerned with mixtures of explosive organic molecules with inorganic matrix molecules.[1-2] The inorganic component functions as the absorber of energy to control the decomposition of the organic component. As the organic part, RDX has received attention since it is a possible pyrotechnics initiator. However, its dissociation pathways are numerous[3-26] due to its responsiveness to the thermal and electronic stimuli used to vaporize and ionize it. While this responsivenes is by design for the original purpose of RDX, it has proven undesirable in the specificity required for its detection. Subsequent efforts to quantify and control its (unavoidable) dissociation pathways made use of laser pulses as the next logical step for energy delivery, which also brought the matrix RDX is in contact with into focus. Passivation of a metal with oxygen is a common occurrence in media containing pure metal, O_2 (g), and laser radiation. Oxide passivated Al nanoparticles[1], aluminum oxide surfaces as substrates[27-29], or Al_xO_y type of anionic gas-phase clusters[30-37] have all been considered as the inorganic part in studies of laser-induced reactivity with organics.

Oxide passivation converts a surface into an insulator where low-energy electrons get captured and linger. Another reaction channel opens up when these electrons subsequently get captured by the various states (e.g. excited, fragmented, etc.) of the organic molecule present in the medium. At this point, time enters the equation governing RDX dissociation as a factor, making it a problem of molecular and electron dynamics.

Our previous density functional theory (DFT) study of a dimeric RDX lattice cell model showed that loss of an electron could result in HONO and NO_2 losses via unimolecular or bimolecular processes.[38] A DFT study on band-gap calculations of α-RDX crystal has produced a band-gap of 3.0-3.1 eV at zero external pressure, less than the calculated vertical ionization energy of a single RDX molecule (10.4-10.9 eV)[39]. Molecular dynamics simulations show that amorphous Al_2O_3 (a-Al_2O_3) have smaller band gaps than the crystalline phase.[40-46] Under the environmental conditions considered, electron-transfer/capture would have a higher probability to occur. [28, 45-46] Effects of an inorganic matrix on the dissociation mechanisms and ionization energetics of RDX can be explored with many different initial conditions.

Availability of molecular pictures of RDX-aluminum oxide interface at any instant after the laser shot would contribute to dynamics simulations as seed geometries.

The electronic structures and geometries of neutral and anionic Al_xO_y clusters have been studied earlier. [47-50] $Al_3O_3^-$ has been the most abundant anion from ablation of Al by the second harmonic (532nm) of a Nd:YAG laser.[49] Its two lowest energy isomers, the rectangle (or book) and the kite, are the smallest clusters that, when combined, provide several charge states for the Al and O atoms. Each isomer offers different positions for possible binding with RDX. In addition, neither isomer contains Al atoms coordinated to more than 3 O atoms i.e. the isomers stoichiometrically represent surface entities with O atoms knocked out by high energy projectiles. Hence, the two isomers of $Al_3O_3^-$ will constitute the reaction partner of RDX in current study.

The neutral RDX isomeric structures are well-known.[51] The stable α-RDX crystal is represented by the EAA-*chair* conformer (RDX I).[52] A less stable RDX polymorph, β-RDX is shown to consist of AAA-*chair* conformer (RDX V).[53] The α-RDX crystal has been shown to convert to γ-RDX under pressure, consisting of RDX I and V.[54] In current work, in addition to RDX-I and RDX-V, slightly higher energy isomers RDX-II (AEE-*chair*), RDX-III (EAA-*twisted boat*), and RDX-IV (unstable, AEE-*boat*) are considered in order to address the pressure and energetic effects of ablation.

Within the scope of the representative species chosen, the objective of current work is to find the final structures arising from *weak* interactions between five different RDX isomers and two different $Al_3O_3^-$ isomers. This gives a total of ten pairings each with conformational subclasses. Only complexes with weak interactions will be addressed. The interaction type/strength, factors governing these interactions and commentary on the electron delocalization will follow.

Methods:

The two lowest energy $Al_3O_3^-$ cluster structures have been studied theoretically, previously.[48] The lowest energy "rectangle" isomer of $Al_3O_3^-$ offers trivalent and divalent Al sites for N–O···Al, and N···Al interactions and O^{2-} sites for C-H···O, and $N(O_2)$···O interactions with RDX. The "kite" isomer offers trivalent, divalent and monovalent Al sites as well as O^{2-} and O^{1-} sites. The RDX isomers I, II, III, and V are characterized as AAE-*chair* (C_s), EEA-*chair*

(C_s), EAA-*twisted boat* (C_1), and AAA-*chair* (C_{3v}) conformations, offering 2, 2, 3, and 1 unique NO_2 sites for binding, respectively. The heterocyclic rings have several H atoms available for C-H⋯O interactions except in the AAA-*chair* (C_{3v}) RDX conformer, in which only 1 equatorial and 1 axial *unique* H atom are present. A fifth albeit unstable (when free) isomer we called RDX IV also arose (AAA-*boat* (C_s)) during optimizations.

Multicenter interactions are formed in the starting geometries. Initial orientations were chosen such that **a)** the N−N bonds are polarized by Al(center)−O, Al(apex,corner)−O, and Al(tail)−O bonds aligned parallel to them, or **b)** the (O−N)−O⋯Al interactions were introduced, or **c)** the C−H⋯O interactions were facilitated. The starting $[RDX \cdot Al_3O_3]^-$ geometries were optimized at PBE0/TZVP(D3) level of theory.[55-58] The binding energies were corrected for the basis set superposition error (BSSE), by the Counterpoise (CP) method [59] and deformation at the PBE0/TZVP(D3) level. Local minimum structures confirmed by positive frequencies (computed with PBE0/TZVP method) were used as input for PBE0/Def2-TZVPP(D3)[60] energy calculations. For charge analysis, Hirshfeld[61] and Mulliken[62] charges were calculated at the PBE0/Def2-TZVPP(D3) level. In addition, iterative Hirshfeld (Hirshfeld-I)[63] charges are calculated using the PBE0/Def2-TZVPP(D3) electron density using Multiwfn[64] program. Natural population analysis (NPA) is performed by the NBO 7.0 program[65] utilized through the ORCA[66-67] program. Vertical detachment energies were calculated at the RHF IP-EOM-DLPNO-CCSD level using PBE0/TZVP(D3) geometries. The calculations were performed using the ORCA program unless otherwise noted.

The intermolecular interactions among the charge-dipole complexes were quantitatively and qualitatively studied using Noncovalent Interaction analysis (NCI)[68] and Independent Gradient Model analysis based on Hirshfeld partition of density (IGMH)[69] methods using the wavefunctions from the PBE0/Def2-TZVPP (D3) calculations in Multiwfn program[64]. The Amsterdam Density Functional (ADF) program[70-71] was used to perform Interacting Quantum Atoms (IQA)[72-74], Energy Decomposition Analysis-Natural Orbitals for Chemical Valence (EDA-NOCV)[75] and Quantum Theory of Atoms in Molecules (QTAIM)[76-77] analyses. For EDA-NOCV and QTAIM analyses PBE0/TZ2P with scalar relativity and very good energy convergence criteria were used.
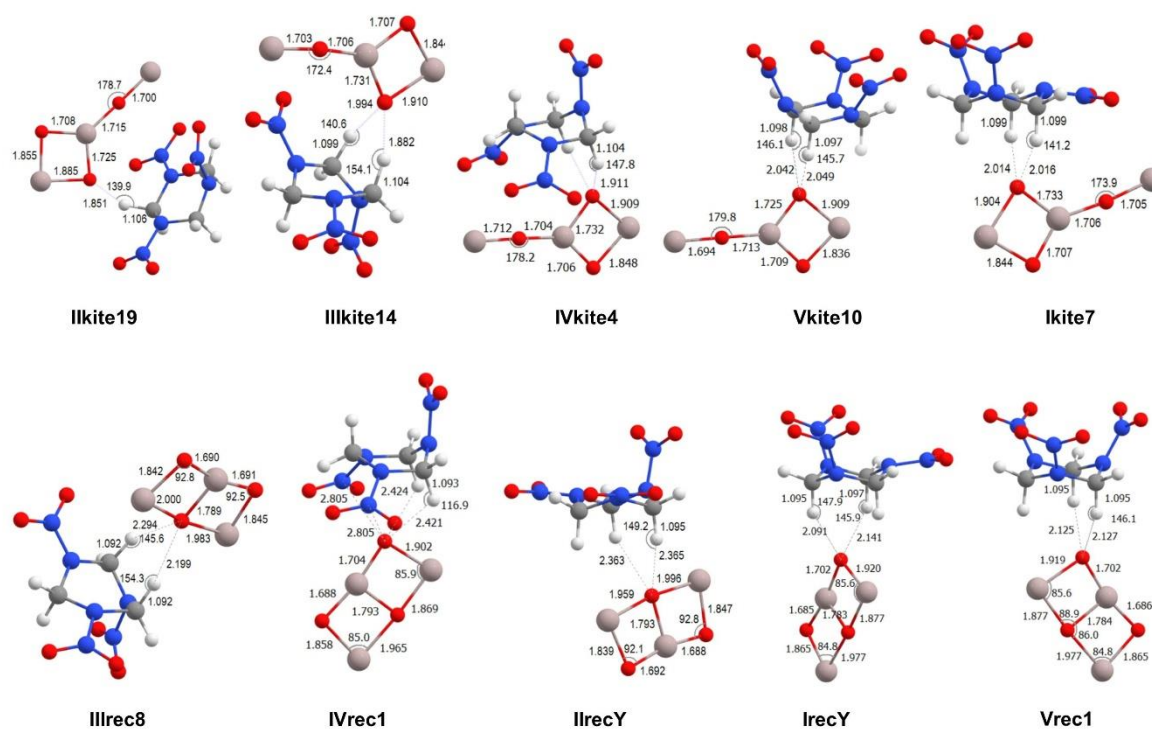
Results:

Structures

Figure 1. Structures of RDX complexes with $Al_3O_3^-$ (*kite*) and $Al_3O_3^-$ (*rec*) calculated using PBE0-D3/TZVP method. The rightmost structures are the lowest energy conformers, increasing in energy from right to left.

The complexes (Figure 1) are optimized from initial orientations with (RDX) C–H···O ($Al_3O_3^-$) interactions and interactions where the RDX lowest unoccupied molecular orbitals (LUMO) and $Al_3O_3^-$ highest occupied molecular orbitals (HOMO) were mismatched.[78] Within the RDX···$Al_3O_3^-$ (*kite*) complexes, the O atoms in the kite head make the connection to H atoms of RDX. RDX isomers I, II, and V have a "H-rich side" and a NO_2-rich side. When the kite head connects to these isomers from the H-rich side, more stable complexes are produced.

The H atoms making these connections are axial with the exception of IIkite19. Low energy complexes exhibit two H-bonds to the kite head O atom (O_{corner}). When the Al atom at the apex of the kite structure (Al_{apex}) is directed towards the RDX ring, the complexes are more stable than those with stacked kite tail-RDX conformations.

Rectangular $Al_3O_3^-$ isomer also prefers to form H-bonds from *below* RDX. The O_{corner} atoms are the preferred locations for the H-bond, rather than the three-coordinated O_{center}. Similar to the kite complexes, RDX isomer III or its unstable version, RDX IV, form higher energy complexes than RDX I, II, or V. When RDX III, originally having two axial and one equatorial NO_2 groups, interacts with $Al_3O_3^-$, one of the axial NO_2 groups converts to equatorial conformation.

Both RDX$\cdots Al_3O_3^-$ (*kite*) and RDX$\cdots Al_3O_3^-$ (*rec*) complex sets are thinly populated and no RDX isomer dominates. These are the unreacted "leftovers" produced by the optimization scheme used in current work which is not statistical. Most complexes have undergone reactions the subject of which is the topic for a subsequent publication. The CD complexes present a glimpse into the minutae of binding between RDX and aluminum oxide anions and will be subject of focus as such.

| | PBE0 D3/def2TZVPP | | | qRDX/e | | | | RHF IP-EOM-DLPNO-CCSD | PBE0 D3/TZVP | | | PBE0/TZ2P | |
	Erel	R(C)H-O ave./A	Dipole Mom./Debye	Hirshfeld	Hirshfeld-I	Mulliken	NPA	VDE/eV	Binding Energy	BSSE	DEgeoprep	Binding Energy	DEgeoprep
IIkite19	18.6	1.851	16.0	-0.061	-0.073	-0.087	-0.048	2.5	-15.6	2.1	3.0	-9.7	3.0
IIIkite14	4.5	1.938	9.4	-0.125	-0.077	-0.097	-0.042	3.1	-29.2	2.3	4.6	-23.9	4.3
IVkite4	3.3	1.912	11.2	-0.086	-0.093	-0.101	-0.048	3.4	-30.6	2.6	4.8	-23.2	4.7
Vkite10	0.9	2.046	4.5	-0.248	-0.134	-0.126	-0.057	3.5	-33.3	1.9	2.4	-29.7	2.4
Ikite7	0	2.015	5.8	-0.171	-0.103	-0.116	-0.041	3.0	-33.9	2.3	3.3	-28.5	3.6
kite			8.6					2.2					
IIIrec8	10.4	2.247	5.0	-0.173	-0.186	-0.074	-0.040	3.5	-18.8	1.2	3.8	-15.4	2.9
IVrec1	7.2	2.423	12.5	-0.132	-0.080	-0.085	-0.026	3.9	-21.8	2.1	2.8	-17.4	2.1
IIrecY	6.5	2.364	2.9	-0.203	-0.221	-0.078	-0.067	3.7	-24.4	1	1.6	-20.7	1.4
IrecY	3.6	2.116	7.4	-0.210	-0.121	-0.106	-0.047	3.9	-26.6	1.2	1.8	-22.9	2.1
Vrec1	3.2	2.126	6.7	-0.208	-0.120	-0.101	-0.045	3.9	-26.9	1.3	1.8	-23.4	2.0
rec			2.7					3.0					

Table 1. Relative energies, *average* H-bond distances from kite/rec O atom to the (C-)H atom of RDX isomers, charges on the RDX part of the RDX$\cdots Al_3O_3^-$ complexes, dipole moments (Debye), vertical detachment energies (VDE), and binding energies are shown. All energies except VDE are in kcal/mol. The binding energies include the deformation energy correction (DEgeoprep). Basis set superposition errors are presented (not included) in addition to the binding energies calculated using PBE0/TZVP method. The PBE0/TZ2P energies were calculated

as Total Bonding Energy with the Binding Energy Analysis module of the ADF program on the PBE0/TZVP geometries. This is the only method where the core electrons are included.

All of the RDX$\cdots$Al$_3$O$_3^-$ complexes are H-bond complexes, with two such apparent interactions in each complex except IIkite19. Table 1 shows that the average O$\cdots$H distances among the RDX$\cdots$Al$_3$O$_3^-$ (*rec*) are all longer than 2 Å, longer than most of those found in the RDX$\cdots$Al$_3$O$_3^-$ (*kite*) complexes.

Structural Effects of Complex Formation

When RDX and Al$_3$O$_3^-$ form complexes, the N-N bonds are shortened, all C-N and N-O bonds are lengthened by various degrees in RDX. All O-N-O angles are widened by 0.4 to 1.8 degrees. (Table S1-S3) The changes are more noticeable in RDX$\cdots$Al$_3$O$_3^-$ (*kite*) isomers. Some exceptions in C-N distances occur in the RDX III and RDX IV. The structural changes do *not* always mimic the effects of the RDX$\rightarrow$[RDX]$^-$ transition: in both [RDX II]$^-$ and [RDX III]$^-$ an axial -NO$_2$ group pops off the ring rather than get close to it.[79] The ring structures of [RDX]$^-$ do not simply "breathe out" as in the complexes in current work but form patterns where some C-N bonds become longer and some shorter.

Complex formation between RDX V and Al$_3$O$_3^-$ mimics the structural effects of RDX$\rightarrow$[RDX]$^-$ transition in terms of C-N and N-O bond lengths but not in N-N lengths or O-N-O angles: RDX$\cdots$Al$_3$O$_3^-$ interactions have localized effects on RDX. The same is true for the Al$_3$O$_3^-$ isomers: the O atom involved in the H-bond interaction is distanced from the Al atoms it is bonded to, causing these Al atoms to compensate for the electron loss by forming tighter bonds to other neighboring O atoms. The structural effects of complex formation on RDX depend on the NO$_2$ and ring conformations in addition to the nature, number and position of the interactions.

The weak interactions were not possible with O$_{tail}$ in kite and Al$_{center}$ in rec. No complex formed and remained as a complex where *both* O$_{corner}$ atoms were involved in H-bonds i.e. the kite/rec was lying flat underneath the RDX. This was due to the O 2p orbital alignment in the Al$_3$O$_3^-$ HOMO which is parallel to the molecular plane. Dangling O atoms or -OH groups on a typical Al$_2$O$_3$ surface would offer more three dimensionality. Still, the way the Al$_3$O$_3^-$ isomers oriented

themselves underneath the RDX is reminiscent of the surface O positions of the O-terminated γ-Al_2O_3 surface.[80] Lastly, no strong Al$\cdots$N type complexes were produced because such an alignment in close proximity resulted in *reacted* complexes *in silico* which will be the subject of a subsequent publication.

RDX-Al$_3$O$_3^-$ interactions: Binding Energies

All complexes are within an 19 kcal/mol energy interval (Table 1). All energies are ordered relative to the lowest energy isomer (Ikite7); RDX$\cdots$Al$_3$O$_3^-$ (*kite*) complexes are lower in energy than the RDX$\cdots$Al$_3$O$_3^-$ (*rec*) complexes except IIkite19. Previous experimental and theoretical work[30,48] on Al$_3$O$_3^-$ have proposed that Al$_3$O$_3^-$ (*rec*) is thermodynamically favored over Al$_3$O$_3^-$ (*kite*), which is the kinetically favored product of pulsed laser ablation (532 nm, 7ns) of an aluminum rod. Complex structures with RDX appears to switch the energy ordering of Al$_3$O$_3^-$ (*rec*) and Al$_3$O$_3^-$ (*kite*).

	BEA						NCI		
	Total Orbital Interactions	Electrostatic Interaction	Pauli Repulsion	Steric interaction	Exchange	Total Bonding Energy	attractive	VdW	repulsive
IIkite19	-16.4	-26.3	29.9	+3.6	-30.3	-12.7	0.048	0.020	0.068
IIIkite14	-21.8	-43.8	37.3	-6.5	-47.9	-28.3	0.074	0.005	0.083
IVkite4	-26.1	-49.2	47.4	-1.8	-56.3	-27.9	0.088	0.012	0.085
Vkite10	-16.8	-39.0	23.7	-15.3	-43.4	-32.1	0.048	0.027	0.078
Ikite7	-19.3	-42.8	30.1	-12.7	-48.3	-32.0	0.062	0.042	0.078
IIIrec8	-9.7	-25.9	17.2	-8.7	-28.7	-18.4	0.031	0.024	0.105
IVrec1	-11.6	-31.3	23.5	-7.8	-29.0	-19.4	0.048	0.022	0.128
IIrecY	-11.0	-28.7	17.6	-11.1	-34.6	-22.1	0.036	0.036	0.104
IrecY	-12.7	-31.2	19.0	-12.2	-36.3	-25.0	0.040	0.033	0.104
Vrec1	-12.4	-31.2	18.4	-12.9	-35.5	-25.3	0.040	0.033	0.103

Table 2. Intermolecular interactions and their components between RDX and Al$_3$O$_3^-$, calculated using the Binding Energy Analysis (BEA) and Noncovalent Interaction analysis (NCI). All values from BEA are in kcal/mol. The values for attractive interactions from the NCI are the sums of the $|\,\text{sign}(\lambda_2)\rho\,|$ values for attractive interactions in atomic units (a.u.). The van der Waals (vdW) and repulsive components are calculated and presented similarly.

Isomers Ikite7 and Vkite10 among the RDX$\cdots$Al$_3$O$_3^-$ (*kite*), IrecY and Vrec1 among the RDX$\cdots$Al$_3$O$_3^-$ (*rec*) have the strongest binding. With the exception of Vkite10 and Ikite7, there is a correlation between the relative energy and the binding energy: the most stable complexes are the ones that bind strongest. The PBE0-D3/Def2-TZVPP//PBE0(D3)/TZVP and Binding

Energy Decomposition (BEA)[72-74] method using PBE0/TZ2P//PBE0(D3)/TZVP agree on the order of the binding energies.(Table 2) The RDX$\cdots$Al$_3$O$_3^-$ (*kite*) have higher BSSE values due to the proximity of the RDX and the Al$_3$O$_3^-$ (*kite*). The IVrec1 and IVkite4 have the largest BSSEs indicating that the -NO$_2$ group proximity to Al$_3$O$_3^-$ is part of the reason. The BEA with PBE0/TZ2P has the BSSE problem reduced and still correlates with the PBE0-D3/Def2-TZVPP//PBE0(D3)/TZVP trends in binding energy with P = 0.98. For the PBE0-D3/Def2-TZVPP//PBE0(D3)/TZVP method, there is no correlation between the binding energy (with or without the deformation energy correction) and the BSSE i.e. the BSSE is not being mistaken for molecular interactions.

The deformation energies (ΔEgeoprep) are also larger among the RDX$\cdots$Al$_3$O$_3^-$ (*kite*). Deformation of the RDX structure is the main contributor to ΔEgeoprep in both types of complexes. In complexes IVrec1 and IVkite4, conversion of RDX III to RDX IV has happened. In IIIrec8, an NO$_2$ group has changed conformation slightly, adding to the large deformation energies in Table 1.

As for the components of the (bimolecular) binding energy calculated via the BEA method (Table 2), the total orbital interactions (e.g. electron delocalization, charge-transfer) and the electrostatic interactions are stabilizing and larger among the RDX$\cdots$Al$_3$O$_3^-$ (*kite*). However, the Pauli repulsion term is also larger among the RDX$\cdots$Al$_3$O$_3^-$ (*kite*), bringing the total binding energy into a scale comparable to that of the RDX$\cdots$Al$_3$O$_3^-$ (*rec*). The sum of the electrostatic interactions and the Pauli repulsion terms, i.e. the steric interactions, reveal the shift of balance towards the RDX$\cdots$Al$_3$O$_3^-$ (*rec*). The average steric interaction is -10.5 kcal/mol among the RDX$\cdots$Al$_3$O$_3^-$ (*rec*) while it is -6.5 kcal/mol among the RDX$\cdots$Al$_3$O$_3^-$ (*kite*). The steric interaction even destabilizes IIkite19, at +3.6 kcal/mol.

Direct comparison of Pauli repulsion between Vkite10 and Vrec1, and Ikite7 and IrecY show that the kite tail and proximity of NO$_2$ groups to Al$_3$O$_3^-$ are the apparent reasons for higher repulsion among the RDX$\cdots$Al$_3$O$_3^-$. This is not surprising, considering that Al$_3$O$_3^-$ is an anion. Pauli repulsion and orbital interactions have correlation of P=-0.95, the factors causing the repulsion between the RDX and the Al$_3$O$_3^-$ (*kite*) also are increasing the orbital interactions. There is no correlation like this among the RDX$\cdots$Al$_3$O$_3^-$ (*rec*).
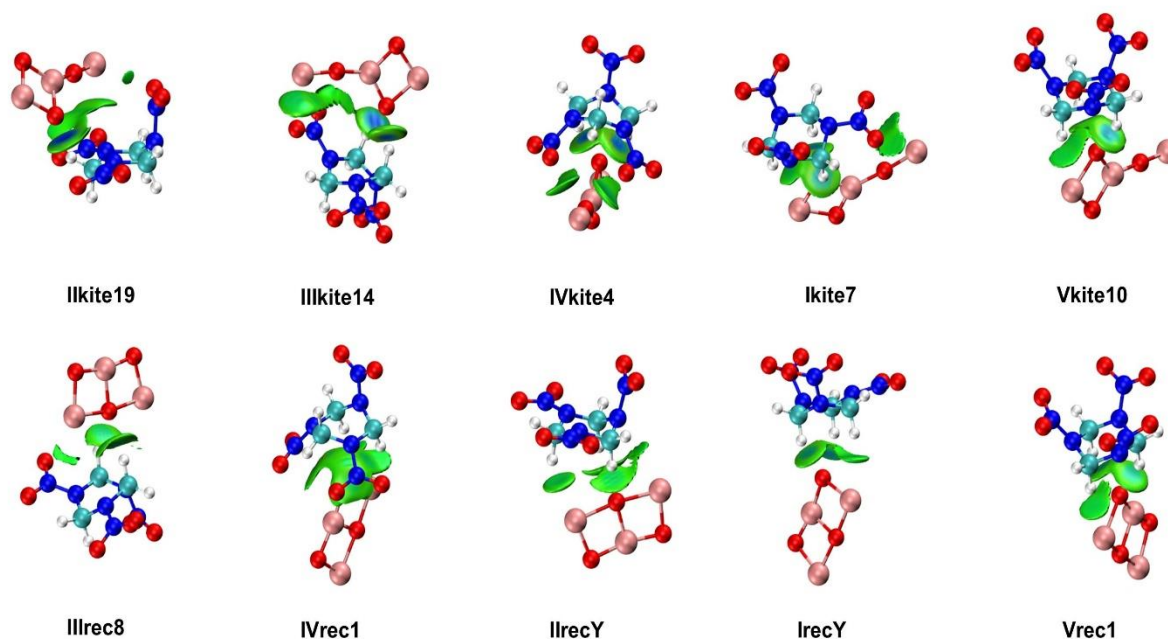
Figure 2. The IGMH maps of the RDX···$Al_3O_3^-$ complexes using the PBE0-D3/Def2TZVPP densities.

RDX-Al₃O₃⁻ interactions: bond specific information from IGMH, NCI, IQA, and QTAIM

The IGMH maps based on Hirshfeld density partition are shown in Figure 2. The IGMH maps show the regions of weak interaction between RDX and $Al_3O_3^-$. The color code given by the sign(λ_2)ρ value changes from light green to blue as the interaction strengthens. The H-bonds are shown with small disks with a blue center. The interaction area between Al_{corner}···NO_2 in IIIrec8, the region beneath Al_{center}-O_{tail}-Al_{tail} train in IIkite19, the elevated region beneath O_{tail} in IIIkite14 appear to be of the weak Van der Waals type.

The NCI and QTAIM analyses of bonding reveal the bond critical points (BCPs, Figure 3) between RDX and $Al_3O_3^-$, to discern whether the interaction areas from the IGMH maps comprise of several bonds with BCPs or are just one big van der Waals (vdW) surface (no BCP). There is an exact agreement between the positions of the IGMH densities and QTAIM and NCI BCPs. In addition to the H-bonds in all complexes, all RDX···$Al_3O_3^-$ (*kite*) isomers have RDX-Al_{tail} interactions in the form of (ON)O···Al_{tail} except for Vkite10 which has a C-H···Al interaction instead. The RDX···$Al_3O_3^-$ (*rec*) isomers stand out with the C-H···Al and N···Al interactions, the latter being over very long distances.
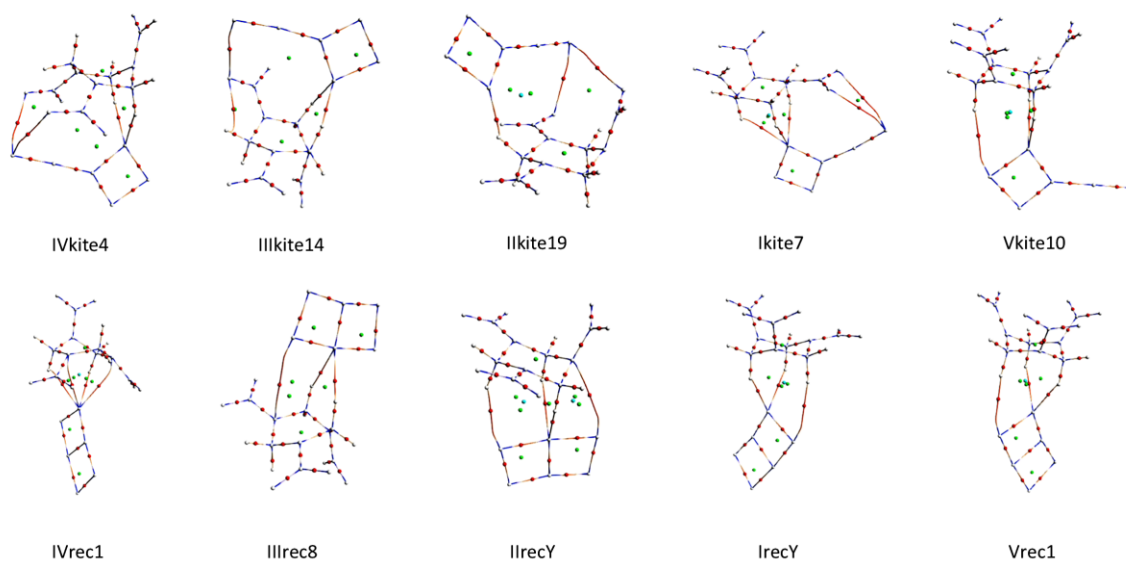
Figure 3. Bond critical points (BCPs) common to both QTAIM and NCI analyses of the RDX$\cdots$Al$_3$O$_3^-$ complexes using the PBE0-D3/Def2TZVPP densities.

Table 3 shows the relative strength of the bonds with BCPs in terms of the Intrinsic Bond Strength Index for Weak interactions (IBSIW) indices in relation to the bond lengths. The IQA analysis, performed on the bonds with BCP information from NCI and QTAIM, allows commentary on charge-transfer character of the interactions. Table 3 also shows sign(λ_2)ρ values from NCI and QTAIM. The order of interaction strength goes as C-H$\cdots$O > (ON)O$\cdots$Al > C-H$\cdots$Al > N$\cdots$Al. The NCI and QTAIM agree on the presence of H-bond interactions and report similar sign(λ_2)ρ values. The relative sign(λ_2)ρ values from NCI and QTAIM decrease, the IBSIW values increase, and bond lengths decrease as relative strength of an H-bond increases with respect to another. For the RDX$\cdots$Al$_3$O$_3^-$ (*kite*) complexes, where the interactions are stronger, the methods agree on all BCPs. For the weakest interactions (Al$_{tail}\cdots$O(NO) type in RDX$\cdots$Al$_3$O$_3^-$ (*kite*) and Al$_{corner}\cdots$H-C and N$\cdots$Al interactions in RDX$\cdots$Al$_3$O$_3^-$ (*rec*) complexes), the QTAIM analysis gives more modest sign(λ_2)ρ values compared to NCI. Also, weaker interactions like N$\cdots$Al are "sensed" differently by QTAIM and NCI. As the interactions get weaker, the difference between the sign(λ_2)ρ values grows due to the differences in assigning and partitioning of the atomic electron densities. A peculiar case is that of the Al$_{corner}\cdots$H-C interaction in IIrecY, which is comparable in strength

atom no.		IBSIW	NCI	QTAIM	Bond Length
	IIIrec8				
16-23	H-Ocenter	1.375	-0.017	-0.015	2.199
21-23	H-Ocenter	1.078	-0.014	-0.012	2.294
	IVrec1				
21-25	H-Ocorner	0.946	-0.012	-0.012	2.421
16-25	H-Ocorner	0.944	-0.012	-0.012	2.424
	IIrecY				
20-26	H-Alcorner	1.013	-0.012	-0.004	2.871
16-23	H-Ocenter	0.912	-0.012	-0.011	2.363
21-23	H-Ocenter	0.906	-0.012	-0.011	2.365
24-5	Al-Nring	0.264	-0.005	-0.003	3.748
	IrecY				
10-25	H-Ocorner	1.697	-0.021	-0.018	2.091
21-25	H-Ocorner	1.508	-0.019	-0.017	2.141
9-24	H-Alcorner	0.771	-0.009	-0.003	2.862
	Vrec1				
10-25	H-Ocorner	1.556	-0.020	-0.017	2.125
21-25	H-Ocorner	1.549	-0.020	-0.017	2.127
9-24	H-Alcorner	0.804	-0.009	-0.004	2.836
	IIkite19				
23-6	H-Ocorner	3.365	-0.036	-0.028	1.851
27-18	O-Altail	1.001	-0.012	-0.005	2.891
27-4	O-Altail	0.266	-0.004	-0.003	3.511
	IVkite4				
21-24	H-Ocorner	2.813	-0.032	-0.025	1.911
16-24	H-Ocorner	2.802	-0.032	-0.025	1.912
13-27	O-Altail	1.019	-0.012	-0.005	2.877
15-27	O-Altail	1.004	-0.012	-0.005	2.883
	IIIkite14				
16-23	H-Ocorner	2.988	-0.034	-0.026	1.882
21-23	H-Ocorner	2.282	-0.027	-0.022	1.994
15-27	O-Altail	1.054	-0.013	-0.005	2.846
	Ikite7				
9-24	H-Ocorner	2.183	-0.026	-0.022	2.014
10-24	H-Ocorner	2.174	-0.026	-0.022	2.016
21-24	H-Ocorner	0.689	-0.010	-0.009	2.481
27-3	O-Altail	0.374	-0.006	-0.003	3.375
27-2	O-Altail	0.364	-0.005	-0.003	3.390
	Vkite10				
9-23	H-Ocorner	1.970	-0.024	-0.020	2.042
21-23	H-Ocorner	1.933	-0.023	-0.020	2.049
10-22	H-Alapex	0.789	-0.009	-0.004	2.854

Table 3. Energetic (sign(λ_2)ρ) and geometric parameters for the atomic interactions in the RDX$\cdots$Al$_3$O$_3^-$ complexes. The IBSIW values are in a.u./Å^2, the NCI and QTAIM sign(λ_2)ρ values are in atomic units (a.u.) and bond lengths are in Ångstroms (Å).

(IBSIW=1.013 a.u./Å^2) to the Al$_{tail}$···O(NO) interactions in RDX···Al$_3$O$_3^-$ (*kite*) complexes when Hirshfeld analysis of density is used (NCI). The QTAIM sign(λ_2)ρ value is -0.004 a.u. while NCI assigns a value of -0.012 a.u., while both methods assign a BCP to the interaction.

Despite the slightly larger distance between Al$_{corner}$ and the H atom, this particular Al$_{corner}$···H-C interaction in IIrecY is stronger than those with smaller Al$_{corner}$···H distances (Vrec1 and IrecY). A reasoning from the point of view of an electrostatic interaction could be that the (AlO)$_{corner}$ unit is an electron rich domain where both Al$_{corner}$ and O$_{corner}$ compete for the proton (or vice versa). When O$_{corner}$ is involved in a strong interaction, it polarizes the electrons towards itself leaving a weaker Al$_{corner}$. In IIrecY and IIIrec8, O$_{center}$, already very taxed in its bonding with the 3 Al atoms and two weak H-bonds, does not present a competition for Al$_{corner}$. Hence Al$_{corner}$ interacts with more affinity with the C-H groups. The case is different for IIIrec8 because there is no H atom in the immediate vicinity of Al$_{corner}$.

The strengths of the H-bonds follow the cluster energy order in RDX···Al$_3$O$_3^-$ (*kite*): the stronger the bond, the higher the cluster relative energy (less stable). The sign(λ_2)ρ grows steadily as the H-bond strength increases: QTAIM values increase "slowly" with IBSIW unlike the NCI values. The difference in response to strength carries over to the Al···O interactions which have their own "slope" against the IBSIW values. The order is somewhat reversed in RDX···Al$_3$O$_3^-$ (*rec*) complexes: the most stable complexes IrecY and Vrec1 have the strongest H-bonds.

Table 2 shows the composition of the interaction energy in terms of attractive, vdW, and repulsive forces per NCI analysis. The absolute value of the (normally negative) attractive interactions are presented. The difference between RDX···Al$_3$O$_3^-$ (*kite*) and RDX···Al$_3$O$_3^-$ (*rec*) lies in the balance between the attractive and repulsive forces: RDX···Al$_3$O$_3^-$ (*kite*) bear stronger attractive and less of repulsive interactions per NCI. The repulsive component arises from *intra*molecular ring critical points (RCPs): one in each Al$_2$O$_2$ half in Al$_3$O$_3^-$ (*rec*) and one in the midst of the RDX isomer heterocyclic ring. These are steric effects. For the RDX···Al$_3$O$_3^-$ (*kite*), there is a repulsive H-O$_{corner}$-H triangle in every isomer except in IIkite19 (only single H-bond). This type of triangle is also present in RDX···Al$_3$O$_3^-$ (*rec*) complexes but since the distances are longer the electron density is lower, placing these points in the vdW

category. Hence, it is the second RCP within the $Al_3O_3^-$ (*rec*) structure that makes the RDX$\cdots$Al$_3$O$_3^-$ (*rec*) complexes more tense within.

		Einter(total)	Vee(exchange)	Coulomb	%exchange		Einter(total)	Vee(exchange)	Coulomb
IIkite19	O22H5	-88.5	-16.7	-71.8	23	Al26O17	-80.4	-10.1	-70.3
IIkite19						Al26O3	-50.2	-2.9	-47.3
IVkite4	O23H20	-73.7	-15.8	-57.9	27	Al26O12	-81.8	-10.1	-71.7
IVkite4	O23H15	-73.3	-15.8	-57.5	22	Al26O14	-81.4	-9.9	-71.5
IIIkite14	O22H15	-74.2	-16.6	-57.7	29	Al26O14	-82.9	-10.8	-72.1
IIIkite14	O22H20	-64.4	-13.1	-51.3	20	Al26O11	-44.8	-0.5	-44.4
Ikite7	O23H8	-52.8	-13.5	-39.3	34	Al26O2	-56.2	-3.8	-52.4
Ikite7	O23H9	-52.2	-13.5	-38.7	26	Al26O1	-55.6	-3.7	-51.9
Ikite7	O24H21	-28.9	-4.5	-24.4	16				
Vkite10	O22H8	-52.1	-12.3	-39.8	31	*Al21H9*	*2.7*	*-6.1*	*8.8*
Vkite10	O22H20	-51.2	-12.2	-39.0	24				
	stdev	17.0	3.6	13.9	5	stdev	16.4	4.2	12.2
	ave	-61.1	-13.4	-47.7	25	ave	-66.6	-6.5	-60.2
IVrec1	O24H20	-29.4	-4.9	-24.6	17	*Al23H20*	*8.3*	*-3.8*	*12.1*
IVrec1	O24H15	-28.4	-4.9	-23.5	17				
IIIrec8	O22H15	-39.2	-8.7	-30.5	22				
IIIrec8	O22H20	-36.6	-7.2	-29.5	20				
IIrecY	O22H20	-27.6	-6.3	-21.3	23	*Al25H19*	*-5.9*	*-10.1*	*4.2*
IIrecY	O22H15	-27.1	-6.3	-20.8	23				
IIrecY	O22H19	-9.2	-0.5	-8.8	5				
IrecY	O24H9	-46.8	-10.8	-35.9	23	*Al23H8*	*-0.7*	*-6.7*	*6.0*
IrecY	O24H20	-40.1	-9.9	-30.2	25				
IrecY	O24H8	-14.0	-2.2	-11.9	16				
Vrec1	O24H20	-43.1	-10.1	-33.1	23	*Al23H8*	*0.3*	*-6.9*	*7.2*
Vrec1	O24H9	-43.0	-10.2	-32.8	24				
	stdev	11.7	3.3	8.5	6	stdev	5.2	2.2	3.0
	ave	-32.1	-6.8	-25.2	20	ave	0.9	-6.7	7.7
All O-H	stdev	20.4	4.7	15.9	6				
All O-H	ave	-45.3	-9.8	-35.5	22				

Table 4. Energetic components (kcal/mol) of interatomic interactions from IQA analysis of the PBE0-D3/Def2TZVPP density in the RDX$\cdots$Al$_3$O$_3^-$ complexes.

The IQA analysis of the *inter*molecular interactions with BCPs (specifically chosen apriori) from both QTAIM and NCI provide a partitioning of the interactions into covalent (exchange) and non-covalent (Coulomb) components. The covalent component is related to the charge transfer involved in H-bonds: the larger this component is, the larger is the charge transfer. Table 4 shows the interaction energies (E_{inter}) and their components in kcal/mol. The E_{inter} varies between -88.5 kcal/mol (IIkite19) and -9.2 kcal/mol (IIrecY). The results also show that all O$\cdots$H interactions have non-zero covalent character ($E_{xc} < 0.0$ kcal/mol) i.e. charge

transfer is involved. The E_{xc} varies between −0.5 (IIrecY) and −16.7 kcal/mol (IIkite19). The coulomb energies are also stabilizing (E_{cl} < 0.0 kcal/mol), varying between −8.8 (IIrecY) and −71.8 kcal/mol (IIkite19). The H-bonding interactions and their components are nearly twice as stable in the RDX···Al$_3$O$_3^-$ (*kite*) than among the RDX···Al$_3$O$_3^-$ (*rec*), with average E_{inter} values of −61.1 vs. −32.1 kcal/mol, respectively. This is also true for the components of E_{inter}: both are twice as stabilizing in RDX···Al$_3$O$_3^-$ (*kite*) than in RDX···Al$_3$O$_3^-$ (*rec*). The standard deviation in the average E_{xc} component is smaller than E_{cl} in both molecule classes. The variation (20.4 kcal/mol) in the average E_{inter} (−45.3 kcal/mol) is due to the variation in the average E_{cl} (15.9 kcal/mol). This is due to the presence of a wide distribution of O···H interactions, the weaker interactions being almost exclusively in the RDX···Al$_3$O$_3^-$ (*rec*) complexes, with no interaction more stable than −46.8 kcal/mol (IrecY). Despite this difference, the weight of the E_{xc} component of E_{inter} is similar in both type of complexes, 20±6 % in the RDX···Al$_3$O$_3^-$ (*rec*) and 25±5% in the RDX···Al$_3$O$_3^-$ (*kite*), since the nature of the interaction is an O···H interaction.

	Eintertotal	Strong sum	Weak sum	Strong%	Weak%	Ecovtotal	cov%	Ecoultotal	coul%
V	-120.8	-103.7	-17.1	86	14	-38.9	32	-81.8	68
Vkite10	-129.7	-87.5	-42.2	67	33	-34.9	27	-94.8	73
Vrec1	-128.4	-90.5	-37.9	70	30	-35.7	28	-92.8	72
I	-112.8	-96.0	-16.7	85	15	-37	33	-76.1	67
Ikite7	-127.9	-81.1	-46.8	63	37	-33.8	26	-94.1	74
IrecY	-124.1	-86.3	-37.9	70	30	-34.9	28	-89.3	72
II	-106.1	-90.2	-15.9	85	15	-34.5	32	-71.6	68
IIkite19	-114.7	-103.3	-11.4	90	10	-32.8	29	-82.0	71
IIrecY	-117.6	-86.6	-31.0	74	26	-34.3	29	-83.2	71
III	-113.4	-86.3	-27.1	76	24	-37.4	33	-76.0	67
IIIkite14	-128.7	-83.5	-45.2	65	35	-33.3	26	-95.5	74
IIIrec8	-117.1	-81.6	-35.6	70	30	-33.8	29	-83.3	71

Table 5. Component analysis of the E_{inter} values from IQA analysis of RDX···Al$_3$O$_3^-$ complexes.

Before complexation with Al$_3$O$_3^-$, the RDX isomers have an H-bonding network of their own. Table 5 shows the sum of the E_{inter} values of this network separated into strong and weak network components. An *equatorial* hydrogen on a chair ring of CNCNCN forms a relatively strong interaction with the oxygen of an *axial* NO$_2$ group. Network of six hydrogens and six oxygens formed this way will be called the *strong* network. Interaction between an axial

oxygen and an axial hydrogen *trans* to the NO_2 is much weaker. The six H and O atoms in this interaction make up the *weak* network. The sum of the E_{inter} of either the strong or the weak network is a stabilizing contribution to the RDX system. Complexation with $Al_3O_3^-$ increases this stabilization. The strong network loses some of its stabilizing effect but the weak network becomes more stabilizing compensating and then adding to the overall stabilization. This is due to an increase in the electrostatic nature of the H-bond interactions in the weak network: when the new H-bonds with the $Al_3O_3^-$ form, the electron density shifts, the H atoms involved in new H-bonds become mere point charges from the point of view of the NO_2 oxygens. The strong network contributes about 85% and the weak network 15% to stabilization in RDX isomers. In the complexes, the contribution of the weak network is doubled to about 30%. An exception is IIkite19 where the strong network gains 5%, bringing it to 90%. The new and strongly covalent H-bond to $Al_3O_3^-$ (*kite*) involves the strong network H atom, increasing the electrostatic interaction between this H atom and the nearby equatorial NO_2 oxygens. It should be noted that RDX (II) has the weakest total network E_{inter}, due to having two equatorial NO_2 groups where RDX (V) has the strongest with all its NO_2 groups being axial. The RDX$\cdots Al_3O_3^-$ (*kite*) isomers are stabilized slightly more than the RDX$\cdots Al_3O_3^-$ (*rec*) when the RDX H-bonding networks are considered. In RDX V$\cdots Al_3O_3^-$ (*kite*), the network total E_{inter} is -129.7 kcal/mol where in RDX V$\cdots Al_3O_3^-$ (*rec*), the value is -128.4 kcal/mol. Differences like this can not explain the twice stabilization in the RDX$\cdots Al_3O_3^-$ interactions among the RDX$\cdots Al_3O_3^-$ (*kite*). While H-bond network may have a role in the RDX$\cdots Al_3O_3^-$ (*kite*) stabilization, it is not the only factor.

The IQA analysis of the Al$\cdots$H interactions shows that while the covalent part is stabilizing, the non-covalent part is repulsive (Table 4). Both H and Al carry partial positive charges which contributes to the repulsive nature of their Coulomb interaction. Only in IrecY (-0.7 kcal/mol) and IIrecY (-5.9 kcal/mol) are these interactions attractive overall. While in IrecY this seems to be the result of a lucky cancellation of the repulsive component, in IIrecY there is a large net electron transfer through the Al$\cdots$H interaction. The average E_{xc} for this type of interaction is -6.5 kcal/mol with a standard deviation of 2.2 kcal/mol. When compared to the H-bonds, among the RDX$\cdots Al_3O_3^-$ (*rec*), the covalent part of the E_{inter} is in the same (-4 to -11 kcal/mol) range as the Al$\cdots$H-C interactions (-3 to -11 kcal/mol) i.e. the Al$\cdots$H-C interactions are of

similar importance as the H-bonds. This is not true for Vkite10 where the H-bonds have twice the covalent character (−12.3 kcal/mol) as in the one Al···H-C interaction (−6.14 kcal/mol).

Despite the very long distances in between (2.8-3.4 Å), relative to those of O···H, the Al···Otail interactions for the BCPs of Ikite7, IIkite19, IIIkite14, and IVkite4 are more stabilizing than any other (Table 4). The covalent part of the interactions is in the same range as in the Al···H-C interactions (−3 to −11 kcal/mol) as are the interaction distances however, the average of the non-covalent part (−67 kcal/mol) is on par with the strongest H-bond among all molecules (IIkite19) (−71.8 kcal/mol).

When the point-charge based E_{cl} component is (E_{pc}) calculated (Table S4) using the Mulliken charges, the average O···H interactions (E_{pc} =−16.9 kcal/mol) appear four times more stabilizing than the Al···O interactions (E_{pc} =−4.1 kcal/mol) in RDX···$Al_3O_3^-$ (*kite*), therefore the large non-covalent part (−67 kcal/mol) in the Al···O interactions are due to multipole effects.

Dipole Moments and Possible Effects on Workfunction:

Multipole effects in the complexes are considered as the charge-dipole and dipole-dipole interactions. The dipole moment of the complex itself is an indication of how much it will interact with the surface it is on or embedded in. In their DFT study of the factors affecting the work function, Φ, of perovskite $SrTiO_3$ surfaces[81], Ma et al. place emphasis on the surface dipole. They inform that placement of electronegative species on a surface or reconstruction of the atomic layer at or beneath a surface results in the change of the surface dipole which may change the work function by a few eV. Acikgoz et al.[80], in their study of phosphorus-doped γ-Al_2O_3 surfaces discovered that surface dipole that formed after doping played an important role on surface reactivity. Specifically, the surface workfunction was altered upon doping, measured at 4.88±0.04 eV prior to doping and 4.16±0.06 eV after. Lee et al.[81] emphasized the importance of surface dipole effects on the workfunction which is quantifiable via UV spectroscopy.[83]

Free $Al_3O_3^-$ (*kite*) has a total dipole moment of 8.6 Debye where $Al_3O_3^-$ (*rec*) has 2.7 Debye (Table 1, Fig. S1, PBE0-D3 Def2-TZVPP). When RDX and $Al_3O_3^-$ (*kite*) form complexes, the

dipole moments span a range from 4.5 to 16 Debye. For the RDX$\cdots$Al$_3$O$_3{}^-$ (*rec*) structures, this range is from 2.9 to 12.5 Debye, larger than the dipole moment of the bare Al$_3$O$_3{}^-$ (*rec*). Complexation increases the total dipole moments in all complexes except for Ikite7 and Vkite10. Even though RDX V and Al$_3$O$_3{}^-$ (*kite*) possess the largest dipole moments, the C-H$\cdots$O and the C-H$\cdots$Al interactions direct the two molecules into a configuration that results in a reduced dipole-moment, 4.5 Debye, the smallest among all the RDX$\cdots$Al$_3$O$_3{}^-$ (*kite*). When the electron withdrawing -NO$_2$ groups are directed away from Al$_3$O$_3{}^-$ (*kite*), there is a cancellation of dipole vectors resulting in a muted overall dipole moment. In IIkite19, the -NO$_2$ groups and the Al$_3$O$_3{}^-$ (*kite*) are on the same side of the heterocyclic ring of RDX, causing augmentation of the dipole moment of the complex. The dipole moment trend among the RDX$\cdots$Al$_3$O$_3{}^-$ (*rec*) can also be explained the same way. Comparison of Vkite10 and Vrec1, Ikite7 and IrecY, IVkite4 and IVrec1 dipoles show that Al$_3$O$_3{}^-$ (*rec*) causes more augmentation when it approaches RDX via O$_{corner}$. The effect of approach via O$_{center}$ has the opposite effect.

In the gas phase and current computation conditions, RDX and Al$_3$O$_3{}^-$ have preferred a relative orientation where the Al$_3$O$_3{}^-$ molecular plane is NOT parallel to the heterocyclic ring system of the RDX but is "cutting through" it. If RDX is to approach a hypothetical Al$_x$O$_y$ surface from above, the Al$_3$O$_3{}^-$ then represents a defect with an O atom protruding from the surface. The dipole moment vectors (Fig. S1) are all aligned in such a manner that they pierce the heterocyclic ring and pass parallel to the Al$_3$O$_3{}^-$ molecular plane into the top surface, by the chemists' convention. Even if a thicker slab of an Al$_x$O$_y$ surface is used in modelling and the Al$_x$O$_y$ loses its contribution to the dipole vector due to cancellations, the charge would remain on the Al$_x$O$_y$ surface, overpowering the effect of the -NO$_2$ groups on RDX. Lee et al.[82], in their review of the effect of surface dipoles on interfacial properties, highlight works that investigate the role of the surface dipole on the workfunction. Work by Alloway et al.[83] show a reduction in the workfunction on the alkane thiolate functionalized metal surfaces as the length of the alkyl group is increased. The effect on the workfunction could be reversed by using alkane thiolates modified with polar groups at the tail, far from the surface. Complexes IIrecY and IIIrec8 have nearly all the magnitude of the dipole moment on a single axis, passing through the RDX moieties and the (AlO)$_{center}$, as if parallel to the surface normal. However, they would not induce as much an effect on the workfunction as could IIkite19, which has a magnitude of 6.0 Debye in the same direction, the largest of all the complexes. One could then expect a *reduction* on the Al$_x$O$_y$ workfunction upon complexation with RDX. Real effect on the

workfunction would also depend on coverage, surface morphology, temperature and external electric fields, warranting systematic DFT simulations with larger systems as future work.

Charge-Transfer: Charge Analysis

Table 1 summarizes the charges transferred, computed by different methods. The atomic Δq maps created using the Hirshfeld charges, which are insensitive to changes in basis set, are shown in Figure 4 (data in Tables S5 and S6). The Δq for each atom is represented by a color scale from red (most charge gained) to blue (most charge lost). There is a selectivity in which NO_2 group acquires the negative charge among the $RDX\cdots Al_3O_3^-$ (*kite*) complexes, which seems not to be present among the $RDX\cdots Al_3O_3^-$ (*rec*). Comparison of Ikite7 to IrecY, Vkite10 to Vrec1, IVkite4 and IVrec1, and IIIkite14 and IIIrec8 shows that the NO_2 groups close to the $(AlO)_{tail}$ moiety of $Al_3O_3^-$ (*kite*) do not get as much electron density as they would be in $Al_3O_3^-$ (*rec*).

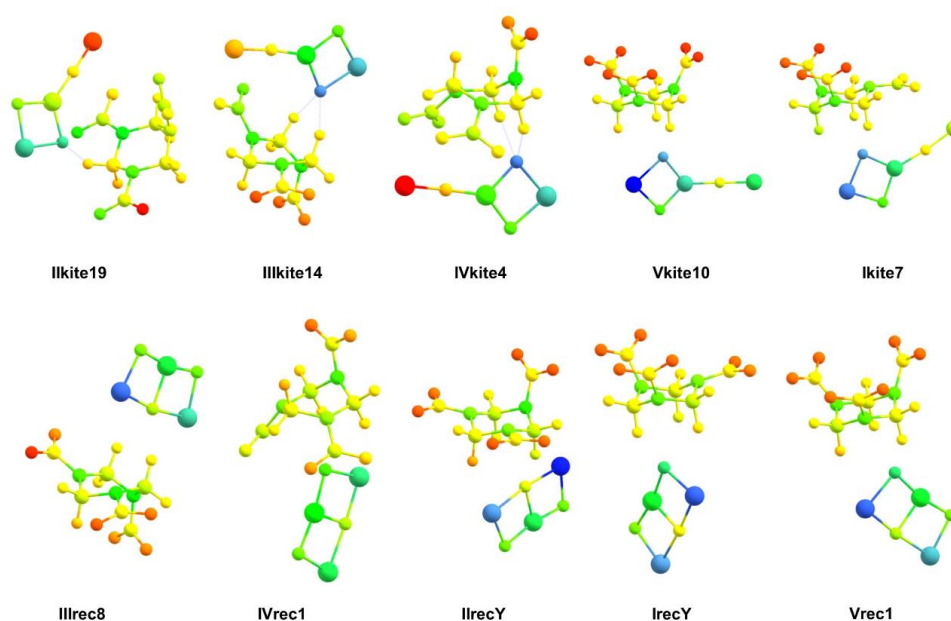**Figure 4.** The atomic Δq maps of the $RDX\cdots Al_3O_3^-$ complexes created using the Hirshfeld charges from (data in Tables S5 and S6) the PBE0-D3/Def2TZVPP densities. The Δq for each atom is represented by a color scale from red (most charge gained) to blue (most charge lost).

The Hirshfeld Δq maps (Fig. 4) also show that some Al atoms have an intense gain of electron

density (red, IVkite4, IIkite19, and to some extent, IIIkite14) and some have lost quite a bit (dark blue, Vkite10, Ikite7, and all RDX$\cdots$Al$_3$O$_3^-$ (*rec*) complexes except IVrec1). The former are the Al$_{tail}$ atoms involved in the BCPs, the latter are those involved in the Al$\cdots$H-C bonding. The RDX H atoms close to an Al atom exhibit yellow-orange hues in Figure 4, indicating acquisition of a larger amount of electrons ($\Delta q<0$) than the other H atoms which remain yellow i.e. at the negatively charged baseline (Δq=-0.010-0.000 e).
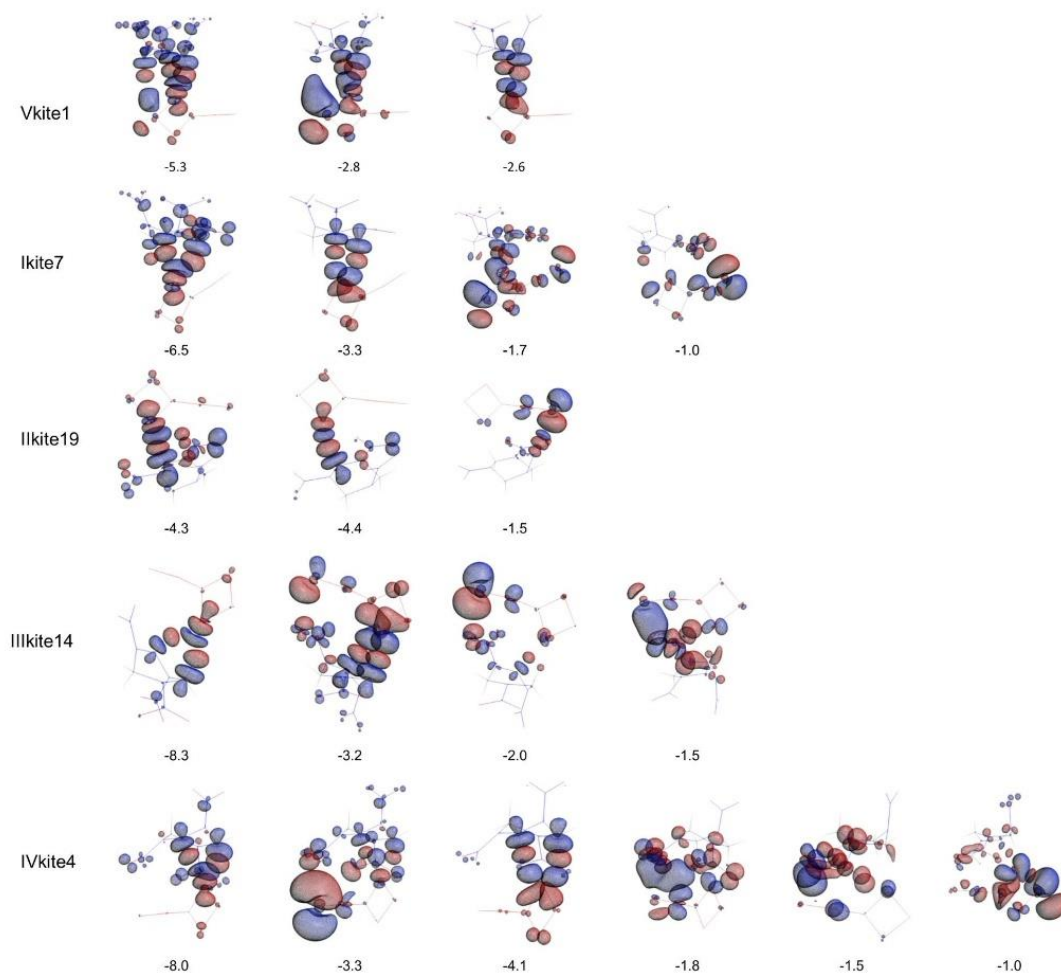

Figure 5. The EDA-NOCV orbitals for the RDX$\cdots$Al$_3$O$_3^-$ (*kite*) complexes from the PBE0-D3/TZ2P densities. The electron density departs the orbitals in red and travels to the orbitals in blue. The orbital interactions with energies (ΔE_{orb}) ≥ 1.0 eV and eigenvalue > 0.1 are shown. The interactions with the largest eigenvalues are placed on the left column, decreasing towards the right. The illustrations contain 50% of the deformation density. The ΔE_{orb} are also listed in kcal/mol.
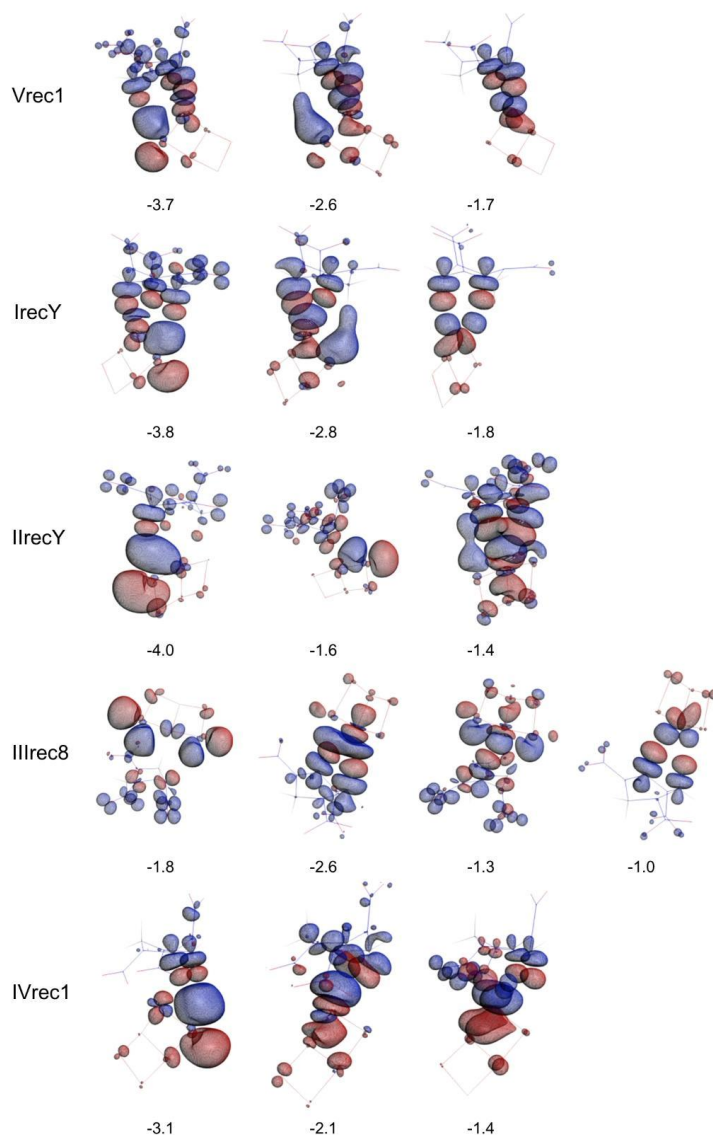
Figure 6. The EDA-NOCV orbitals for the RDX···Al$_3$O$_3^-$ (*rec*) complexes from the PBE0-D3/TZ2P densities. The electron density departs the orbitals in red and travels to the orbitals in blue. The orbital interactions with energies (ΔE_{orb}) ≥ 1.0 eV and eigenvalue > 0.1 are shown. The interactions with the largest eigenvalues are placed on the left column, decreasing towards the right. The illustrations contain 50% of the deformation density. The ΔE_{orb} are also listed in kcal/mol.

Charge-Transfer: EDA-NOCV

Figures 5 and 6 show the EDA-NOCV orbitals from which the electron density departs (red) and then travels to (blue). The orbital interactions with energies (ΔE_{orb}) ≥ 1.0 eV and eigenvalue

> 0.1 are shown. The interactions with the largest eigenvalues are placed on the left column, decreasing towards the right. The illustrations contain 50% of the deformation density. The ΔE_{orb} are also listed in kcal/mol.

The most dominant orbital interactions are the various O(2p)-to-C-H(σ*) type of electron transfer as would be seen in H-bonds[84], indicating a channel of transfer *from* the $Al_3O_3^-$ moiety *to* the RDX. The -N-NO$_2$ groups also receive some of the electron density transferred via H-bonding. The electron transfer is not one directional: all RDX$\cdots$Al$_3$O$_3^-$ (*kite*) isomers have a channel of electron transfer *from* RDX *to* the (AlO)$_{tail}$ of Al$_3$O$_3^-$ (*kite*) (except Vkite10). Isomer Vkite10 has an Al(3p)-to-C-H(σ*) type of interaction which is another channel of transfer *from* the Al$_3$O$_3^-$ moiety *to* the RDX. This is a *non-conventional* H-bonding interaction.[84] This explains the much larger electron transfer in Vkite10: the tail of the Al$_3$O$_3^-$ (*kite*) is not in a position to receive the electrons back. What really makes Vkite10 special among the RDX$\cdots$Al$_3$O$_3^-$ (*kite*) isomers is the presence of a strong orbital interaction between the Al$_3$O$_3^-$ (*kite*) HOMO and the LUMO+3 (MO 61 of C-H (σ*) type) of RDX V (Fig 5, Fig. S2a). Therefore, a sum of the O$\cdots$H-C, Al$\cdots$H-C, and orbital interaction is responsible for the unusual amount of electron transfer to RDX V, especially per Hirshfeld charge analysis.

The electron deformation maps of Vkite10 and of Vrec1 are very similar: the bond-deficient Al$_{head}$ /Al$_{corner}$ is involved in electron transfer *to* RDX. Even though Vkite10 is the only isomer bearing this interaction among the RDX$\cdots$Al$_3$O$_3^-$ (*kite*), it is the dominant component in almost all of the RDX$\cdots$Al$_3$O$_3^-$ (*rec*) complexes (Fig. 6). The first column has both the Al$_{corner}$ (3p) and the O$_{corner}$ (2p) donating electrons to the C-H(σ*) orbitals. There are additional O(2p)-to-C-H(σ*) components in the remaining columns for Vrec1. Hence there are *two* electron transfer channels *to* RDX but no back-transfer of electrons. This is true for most of the RDX$\cdots$Al$_3$O$_3^-$ (*rec*) complexes.

Isomer IIIrec8 is similar to Vkite10 in that there is strong orbital interaction between the HOMO of Al$_3$O$_3^-$ (*rec*) and the LUMO of RDX III (Fig. S2b). While this interaction is the most dominant in IIIrec8, it is not the strongest interaction (-1.8 kcal/mol)(Fig. 6). That title belongs to the H-bonding O(2p)-to-C-H(σ*) interaction between O$_{center}$ and two C-H groups (-2.6 kcal/mol).

The relative strength of orbital interactions reveal that the RDX···$Al_3O_3^-$ (*kite*) isomers have more interactions with $\Delta E_{orb} \geq$ -1.0 eV (than RDX···$Al_3O_3^-$ (*rec*)) having more than 10% contribution to the deformation density. This is due to the activity of the $(AlO)_{tail}$ in $Al_3O_3^-$ (*kite*) in "cycling" of the electrons. Isomer IIkite19 is such an example: while the two most dominant interactions (ΔE_{orb} = -4.3 and -4.4 eV) place electrons into the O atom (of NO_2eq) of RDX closest to Al_{tail} via the $O_{head}(2p)$-to-C-H(σ*) interactions, the third interaction (ΔE_{orb} = -1.5 eV) transfers electrons from that O atom back onto $(AlO)_{tail}$. Isomer Ikite7 NOCV4, IIIkite14 NOCV3, and IVkite4 NOCV2 involve $Al_3O_3^-$ (*kite*) LUMO+1 in addition to the RDX LUMO orbitals in a dominant manner as the electron receiving end. The $Al_3O_3^-$ (*kite*) LUMO+1 also appears in Ikite7 NOCV3, IIIkite14 NOCV2 and NOCV4, and IVkite4 NOCV4 and NOCV5 as a minor constituent.

From a more general perspective, in the RDX···$Al_3O_3^-$ (*kite*), the electron starts its journey from its source, the HOMO of $Al_3O_3^-$, to an excited state of RDX, simultaneously populating an excited state of $Al_3O_3^-$. This transfer requires solely a proper positioning of $Al_3O_3^-$ and RDX at room temperature at which all calculations were run. It would therefore be important to consider excited states of the interacting partners upon separation, which is a possible outcome if energy > $E_{binding}$ is supplied to the system.

Current work has shown that some Al atoms may form bonds with incoming C-H moieties of an organic molecule by *donating* electrons as if it is a Lewis base, in the non-conventional H-bonds. Raghavachari and Das[35] showed the possibility of formation of Al-H bonds in Al-rich $Al_xO_y^-$ type clusters, the hydrides are calculated to be more stable than the hydroxilated clusters by 30-35 kcal/mol by DFT. He et al.[85] detected oxidative dehydrogenation in the reaction of *anionic* aluminum vanadium bimetallic clusters prepared by laser ablation with ethane and *n*-butane using time-of-flight mass spectrometry and DFT calculations. Abstraction of hydrogen from the alkanes were found to be favorable thermodynamically and kinetically. Shi et al.[86] report x-ray and NMR structures of sites in organic crystals where (up to 15) C-H groups are bound to Cl anion via hydrogen binding type interactions. The calculations in current work also reflect the propensity of the C-H bonds towards interaction with anionic species and Al atoms that lack coordination. However, hydride formation did not occur during calculations.

In their work, Wischert et al. inform that $\{^1\text{H}\}$-^{27}Al cross-polarization NMR technique may overlook the presence of the reactive Al sites at defects if the surface has lost its water content.[87] The Al_3O_3^- isomers mimic some of the reactive non-hydrated Al sites on catalytic γ-Al_2O_3 surfaces mentioned therein. The Al atoms involved in interactions with RDX are not Lewis acidic, however, which is a great distinction from the surfaces described. The $\{^1\text{H}\}$-^{27}Al cross-polarization NMR could light up the Al atoms within the H-bonding due to proximity but it would also be interesting to know the contribution of the C-H$\cdots$Al interaction to the chemical shift observed for Al concurrently covalently bound to O atoms.

Concerning the electron transfer on aluminum oxide sites which are anionic not due to hydroxilation but as they are (e.g. Al_3O_3^- kite and rec), one of the findings is the effect of electron transfer to the site geometry and vice versa. Our calculations show that the effects are never localized just on the atom involved in the interactions but translates to the rest of the network, altering distances and charge states within the site because the electron resides in several locations before transfer due to presence of low level of coordination in several Al atoms. This echoes the effect of dehydration in the experiments of Wischert et al. where the ^{27}Al go far from hydrogens due to structural reorganization, becoming spectroscopically invisible in the process.[87] Further, the effect of electron transfer on the receiver of the electron, which in our case is RDX, is also not localized. Therefore it is imperative to identify the atomic groups affected by the interaction and treat the signals from them as a "signal array", correlating atomic positional shifts via e.g. x-ray diffraction with NMR chemical shifts.

Medvedev et al.[28] studied the interaction between trinitrobenzene (TNB) and the Al_2O_3 surfaces using electron paramagnetic resonance (EPR). Radical anions formed and solvent was found to affect the electron transfer rate. It was found that for electron transfer to be observed, much adsorbate was needed and TNB vapor by itself did not create radicals upon adsorption. Bonding between Al atoms and the -NO_2 groups of TNB was suggested to occur. In subsequent work on dehydrated γ-Al_2O_3 by Vasenin et al.[88], it was presented that the surface does not have extra electrons and electron transfer from the surface to the TNB molecular orbitals is unlikely. They attribute the EPR spectra features to presence of atomic oxygen anion. Our calculations do not involve the effect of solvent, TNB has a different orbital architecture than RDX, and our aluminum oxide is an Al-rich anionic cluster where bonding has been deemed not entirely ionic.[48] Therefore it is only natural that our calculations offer different suggestions. Current

work reports partial rather than full electron transfer perhaps as a *prelude* to a reaction. Previous anion photoelectron spectroscopy, time-of-flight mass spectrometry studies[30,50] and calculations[31-37,] on the $Al_3O_3^-$ + xH_2O (x=1-2) systems indicated that the H_2O molecule breaks apart on the Al-rich clusters producing hydroxides and hydrides. Modelling RDX+ $Al_3O_3^-$ + xH_2O system could offer insight into any form of competition between electron transfer and proton abstraction and mutual effects in the future.

Vertical Detachment Energies (VDE):

The experimental electron affinity (EA)[ref] for the $Al_3O_3^-$ (*kite*) and $Al_3O_3^-$ (*rec*) as well as the calculated VDEs for all species are shown in Table 1. The VDE is the electronic energy difference between the neutral and the anion at the anion geometry. By using the RHF IP-EOM-DLPNO-CCSD approach we calculated the *ionization potential* of the $RDX \cdots Al_3O_3^-$ anion at the anion geometry i.e. the VDE. The VDE calculated this way for the bare rectangle and kite isomers are larger than the experimental values by 0.1 eV.

Among the $RDX \cdots Al_3O_3^-$, since the electron resides mostly on $Al_3O_3^-$, one can correlate the VDE $(RDX \cdots Al_3O_3^-)$ – VDE $(Al_3O_3^-)$ with the solvent (RDX) stabilization of the $Al_3O_3^-$ HOMO. All complexes have larger VDEs than the relevant $Al_3O_3^-$ isomer which shows that the $Al_3O_3^-$ HOMO gets stabilized by the RDX isomers. From a wider perspective, this also indicates that upon weak interaction with the organic RDX, the electron would stick more to the "complex".

When RDX isomer V interacts with $Al_3O_3^-$ (*kite*) it *raises* the VDE by 1.3 eV. In the lower limit, interaction of RDX isomer II with $Al_3O_3^-$ (*kite*) *raises* the VDE only by 0.3 eV. The shift in VDE for the interaction between RDX isomers and $Al_3O_3^-$ (*rec*) is in the 1.0-0.5 eV range. One would then expect that, at least initially, the defects would trap the electrons. In amorphous Al_2O_3 films deposited from gas phase, Århammar et al.[43] found evidence of trapped peroxy ions (O_2^x) in the films with one O atom bound to 2 Al atoms and the other O atom bound to one Al atom. They proposed that these have a role in electron trapping within the solid. Current work proposes additional electronic environments in such films which may contribute to the trapping of electrons and supply one of the O atoms (O_{corner}) for peroxy ion formation.

mode	kite	Vkite10	Shift	Ikite7	Shift	IIIkite14	Shift	IVkite4	Shift	IIkite19	Shift
1	64.6	75.1	10.5	87.6	23.0	98.2	33.5	104.5	39.9	79.8	15.1
2	67.2	69.8	2.6	71.9	4.7	67.1	-0.1	83.1	15.9	66.1	-1.1
3	165.2	168.3	3.0	168.8	3.5	171.1	5.9	181.6	16.3	174.1	8.9
4	240.0	243.3	3.2	240.9	0.9	242.9	2.9	247.1	7.1	240.2	0.1
5	325.3	327.1	1.9	326.8	1.5	330.3	5.0	333.6	8.3	337.7	12.5
6	334.8	338.4	3.6	336.9	2.0	336.0	1.1	335.2	0.4	330.7	-4.1
7	485.5	453.9	-31.6	463.4	-22.1	457.3	-28.2	457.6	-27.8	476.0	-9.5
8	550.3	609.9	59.6	557.7	7.4	560.9	10.7	556.0	5.8	546.8	-3.5
9	589.8	567.7	-22.1	604.5	14.8	604.1	14.4	601.5	11.8	595.8	6.0
10	830.9	813.3	-17.5	797.1	-33.8	803.3	-27.6	798.3	-32.5	812.9	-18.0
11	852.5	853.2	0.7	851.3	-1.2	853.1	0.6	851.8	-0.7	852.0	-0.5
12	1063.1	1069.3	6.2	1056.9	-6.2	1061.2	-1.9	1052.7	-10.4	1051.1	-12.0

mode	rectangle	Vrec1	Shift	IrecY	Shift	IIrecY	Shift	IIIrec8	Shift	IVrec1	Shift
1	108.6	113.9	5.3	114.0	5.4	106.9	-1.7	112.0	3.4	126.1	17.5
2	160.8	165.6	4.8	167.3	6.5	163.4	2.6	165.4	4.6	188.5	27.7
3	216.8	210.7	-6.1	208.9	-7.8	184.2	-32.6	179.0	-37.8	218.6	1.8
4	328.0	328.2	0.2	327.8	-0.1	328.2	0.2	329.3	1.4	335.7	7.7
5	370.5	366.8	-3.7	367.1	-3.4	343.4	-27.0	327.9	-42.5	378.4	7.9
6	417.8	418.4	0.6	420.0	2.2	412.3	-5.5	406.6	-11.2	423.8	6.0
7	466.3	437.0	-29.3	434.8	-31.5	467.9	1.6	459.3	-7.0	459.7	-6.6
8	545.6	530.3	-15.3	529.6	-16.0	577.0	31.4	589.7	44.1	545.5	0.0
9	592.5	607.1	14.6	607.2	14.7	595.9	3.4	577.2	-15.3	625.0	32.5
10	691.2	696.6	5.3	696.8	5.5	682.8	-8.4	691.2	0.0	676.3	-14.9
11	743.8	748.2	4.4	748.1	4.4	745.3	1.5	745.3	1.6	745.5	1.7
12	1011.7	1009.0	-2.7	1008.9	-2.8	1016.1	4.4	1014.9	3.2	1004.4	-7.2

Table 6. Vibrational frequencies for the normal modes of the $Al_3O_3^-$ component of the $RDX\cdots Al_3O_3^-$ complexes are shown. Shifts of the frequencies from those of the related bare $Al_3O_3^-$ isomers are also given. All frequencies and shifts are in cm^{-1}. The frequencies are calculated at the PBE0-D3/TZVP level and all structures are at their stationary states.

Vibrational Modes and Frequency Shifts:

Table 6 shows the vibrational frequencies of the $Al_3O_3^-$ part of the complexes and the information on the new *intermolecular* vibrations that emerged upon complexation and interaction. The normal mode vectors for the $Al_3O_3^-$ part of the complexes are shown in Fig. S3. Rather than the frequencies themselves, the directions of the shifts are worth the discussion.

Modes involving the atoms in the interactions with BCPs (Table 3) are shifted. Among the $RDX \cdots Al_3O_3^-$ (*kite*), in IVkite4 and IIkite19 isomers, the modes involving the $(AlO)_{tail}$ moiety shift in frequency. The rest of the isomers respond to the H-bonds formed by their O_{corner} atoms leading to frequency modulations involving this atom. On the other hand, for modes involving separation of Al_{center} and O_{tail}, a frequency shift is not registered at all. For the $RDX \cdots Al_3O_3^-$ (*rec*), out-of-plane mode frequencies are shifted only in IVrec1 due to interactions with two NO_2 groups. Vibrations involving O_{center} and Al_{center} are strongly shifted in IIrecY and IIIrec8 since they form H-bonds via O_{center}.

The $Al_3O_3^-$ (*kite*) presents 12 (unscaled) normal modes between 64 and 1064 cm^{-1}. The lowest frequency mode at $\nu_1 = 64.6$ cm^{-1} and modes between 486 and 831 cm^{-1}, which are also in-plane modes, are shifted by various extents upon complexation. The $\nu_1 = 64.6$ cm^{-1} increases by 11-40 cm^{-1}, $\nu_7 = 486$ cm^{-1} decreases by 10-32 cm^{-1} and $\nu_{10} = 831$ cm^{-1} decreases by 17-34 cm^{-1}. Mode ν_1 is the in plane tail bending mode whose frequency rises in the order Vkite10 < IIkite19 < Ikite7 < IIIkite14 < IVkite4. This mode becomes a *mixed* mode in IIIkite14 and IIkite19. Based on the electron deformation maps of Figure 5, the largest difference in electron density in the tail region is expected mostly in IVkite4, then in the order IIIkite14, IIkite19, Ikite7, and Vkite10. The shifts in frequencies of tail motion are therefore a response to kite tail – RDX interactions. Mode ν_7 distorts the kite head via the asymmetric stretch of the O_{corner}-Al_{head}-O_{corner} moiety. Its frequency drops in the order IIkite19 < Ikite7 < IVkite4 < IIIkite14 < Vkite10 i.e. complexation affects the kite head most in Vkite10. The electron deformation maps show not one but two dominant electron transfer mechanisms from the kite head in Vkite10 so this is expected. Mode ν_7 is also mixed for Vkite10 and IVkite4. Mode ν_{10} is the asymmetric stretch of the O_{corner}-Al_{center}-O_{corner} moiety. Excitation of this mode indicates change in the electron density between the Al_{center} and the O_{corner} atoms, opening up the kite head. Here, Ikite7 and IVkite4 have similar frequency shifts at about ~-33 cm^{-1}, and IIkite19 and Vkite10 have similar shifts of ~-18 cm^{-1}. This response best correlates (P=-0.95) with the number of contributions including orbitals of the kite $(AlO)_{tail}$ moiety in Fig. 5. It is important to note that the kite tail orbitals are never the sole contributor in any eigenfunction, they are always accompanied by the orbitals of the Al_2O_2 head.

Isomer IVkite4 exhibits shifts in two out-of-plane modes, $\nu_2 = 67$ cm^{-1} and $\nu_3 = 165$ cm^{-1}. Mode ν_2 is the movement of Al_{tail} and Al_{apex} simultaneously in the same direction on the σ_v' plane of

the molecule while all other atoms move in the opposite direction. Mode ν_3 is the movement of the O_{tail} and the two O_{corner} atoms in the opposite direction on the σ_v' plane. The mode frequencies increase as a response to electrons being transferred to the tail region via the two $Al_3O_3^-$ (*kite*)-NO_2 interactions.

The $Al_3O_3^-$ (*rec*) presents 12 normal modes between (unscaled) 108 and 1012 cm^{-1}. Complexation results in mixing of two (in IIrecY and IIIrec8) up to six modes (in IVrec1) with those of RDX. No vibration is shifted consistently in a certain direction for all isomers. Modes ν_1, ν_2, and ν_{10} are shifted in IVrec1 only. Modes ν_1= 109 cm^{-1}, ν_2= 161 cm^{-1} are low frequency out-of-plane modes in $Al_3O_3^-$ (*rec*) that jump by 17.5 and 27.7 cm^{-1} in IVrec1. The former can be described as the book wing flapping due to bending of the Al_{corner}-O_{center}-Al_{corner} moiety in the plane 90 degree to that of the molecular plane. The latter is the twisting of the O_{corner} atoms out of the plane of the molecule. Finally, ν_{10} is the Al_{center}-O_{center} stretch. Modes ν_1, ν_2 are shifted to higher frequencies due to the $Al_3O_3^-$ (*rec*) - NO_2 interactions which are out-of plane from the $Al_3O_3^-$ (*rec*) perspective.

Isomers IIrecY and IIIrec8 are the only two isomers that exhibit large drops in frequency in modes ν_3= 217 cm^{-1} and ν_5 = 370 cm^{-1}. Both modes involve the in-plane motion of the Al_{center}-O_{center} moiety as a single entity. Due to syphoning of electrons from this region via the C-H$\cdots O_{center}$ bonds, the relationship of O_{center} with the Al atoms it is in contact with would weaken resulting in the calculated shifts.

Modes ν_8= 546 cm^{-1} and ν_9 = 592 cm^{-1} are shifted in all RDX$\cdots Al_3O_3^-$ (*rec*) with exceptions. Mode ν_8 is a symmetrical combination of the two Al_{corner}-O_{corner} stretching modes w.r.to the σ_v' plane of the molecule. Mode ν_9 is the ring opening mode seeming as O_{corner}-Al_{corner}-O_{center} asymmetrical stretch. These modes would be excited because of the geometric changes induced on the Al_{corner}-O_{corner} and Al_{corner}-O_{center} bonds. Upon H-bonding, antisymmetry is introduced into these bonds both w.r.to the σ_v' plane. The Al_{corner}-O_{corner} bond with the C-H$\cdots O_{corner}$ interaction becomes longer compared to its counterpart across σ_v'. In IIrecY and IIIrec8, the O_{corner}-Al_{corner} distances become shorter, hence the increase in frequency by 30-45 cm^{-1}. The O_{corner}-Al_{corner}-O_{center} geometry is altered towards extension of the O_{corner}-Al_{corner} bond while shortening the Al_{corner}-O_{center} bond resulting in an asymmetric stretching effect per mode ν_9.

The largest change in geometry from the $Al_3O_3^-$ (*rec*) occurs in IVrec1 due to the additional -NO_2 effect on the structure.

The $Al_3O_3^-$ part of the clusters will contribute to the 50-1100 cm^{-1} range of the IR spectrum. If the vibrations are binned for every 100 cm^{-1} for a general view, ranges 0-199 cm^{-1}, 600-799 cm^{-1}, 1000-1099 cm^{-1}, 1400-1699 cm^{-1}, and 2800-3099 cm^{-1} will be populated with more signal after the shifts brought on by complexation (Fig. S4).

	Vkite10	Ikite7	IIkite19	IIIkite14	RDX V	RDX I	RDX II	RDX III		V	I	II	III
			2887.8				3212.2					-324	
	3016.0	2994.9	2998.1	2916.7	3092.1	3037.8	2977.3	3075.6		-76	-43	21	-222
	3028.7	3005.6	3018.9	3000.2	3092.2	3038.8	3048.3	3106.0		-69	-33	-29	-106
	3044.4	3099.6	3032.3	3050.6	3097.8	3109.6	3055.5	3138.2		-53	-10	-23	-25
									Average	-73	-38	-26	
RDX-kite	107.8	118.8	-	107.4									
				123.6									
	Vrec1	IrecY	IIrecY	IIIrec8	RDX V	RDX I	RDX II	RDX III		V	I	II	III
	3036.3	3002.1	2915.0	3028.0	3092.1	3037.8	2977.3	3075.6		-56	-36	-62	-48
	3058.8	3036.7	3061.8	3086.7	3092.2	3038.8	3048.3	3106.0		-33	-1	14	-19
	3068.2	3062.1	3067.4	3092.8	3097.8	3109.6	3055.5	3138.2		-30	-48	12	-19
									Average	-32	-24	13	-19
RDX-rec	95.8	91.8	84.4	65.8									

Table 7. Vibrational frequencies for the normal modes of the C-H stretching frequencies of the RDX component of the RDX$\cdots Al_3O_3^-$ complexes are shown. Frequencies of new intermolecular normal modes are given as *RDX-kite* and *RDX-rec*. Shifts of the C-H frequencies from those of the related bare RDX isomers are also given. All frequencies and shifts are in cm^{-1}. The frequencies are calculated at the PBE0-D3/TZVP level and all structures are at their stationary states.

The vibrational frequencies of the RDX part indicate a general weakening. Modulations in the C-H stretching frequencies are, ideally, indicators of the C-H$\cdots$O and C-H$\cdots$Al interactions. Table 7 shows the vibrations with ~3000 cm^{-1} which are the stretching modes of the axial C-H groups usually involved in the C-H$\cdots$O and C-H$\cdots$Al interactions. Local symmetry dictates anti and parallel stretching modes for two symmetrical C-H bonds making up 2 of the 3 modes. These designations live on in $Al_3O_3^-$ (*rec*) with RDX V and II, and in $Al_3O_3^-$ (*kite*) with RDX V, I, and II. Complexes with RDX IV were not considered in this analysis. The shifts are calculated between similar modes.

The C-H stretching frequencies are reduced in the RDX$\cdots$Al$_3$O$_3^-$ (*kite*) complexes in accordance with the strength of their H-bonds. A discrepancy arises between Vkite10 and Ikite7 where the shifts are larger for Vkite10 even though the H-bonds are weaker than Ikite7. This may be the effect of the electron transfer to RDX V via the C-H$\cdots$Al interaction nearby. The C-H moieties close to the Al atom in Vkite10 and Ikite7 vibrate with less energy, shifting by -53 and -10 cm^{-1}, respectively. A shift of -53 cm^{-1} is significant however caution must be exercised. This may not be solely attributed to the C-H$\cdots$Al interactions since IIkite19 and IIIkite14 also show weaker vibrations in C-H moieties which play no apparent part in H-bonds or C-H$\cdots$Al interactions. In IIkite19, the C-H frequency for the H-bonding equatorial C-H moiety is reduced by ~324 cm^{-1} from 3212 to 2888 cm^{-1}. An exception arises to the general weakening trend in this isomer where the axial C-H moiety on the same C atom *gains* in frequency by 20 cm^{-1}. Such drastic changes are also seen in IIIkite14 where the C-H stretching frequency is reduced by 222 and 106 cm^{-1} in the short and longer H-bonds, respectively.

The RDX$\cdots$Al$_3$O$_3^-$ (*rec*) complexes exhibit smaller shifts in the C-H stretching region. In addition, there are the C-H$\cdots$Al interactions in all but IIIrec8. The average shifts for the C-H moieties involved in the C-H$\cdots$O interactions range from -32 to +13 cm^{-1}. The positive shift happens in IIrecY, in which the C-H$\cdots$Al interaction is strongest, causing a shift of -62 cm^{-1} in the C-H vibration within. In this isomer, the C-H$\cdots$O interactions are the weakest, not adding much of a pull between the O$_{center}$ in Al$_3$O$_3^-$ (*rec*) and the C-H moiety. Another oddity is the IIIrec8 where the axial C-H with no H-bonds exhibits a -48 cm^{-1} shift in its stretching frequency while the average asymmetrical stretching C-H frequency (for the two C-H moieties in the H-bonds with O$_{center}$) has a shift of -19 cm^{-1}. This has to do with **a)** the weakness of the H-bonds of IIrecY compared to IIIrec8 and **b)** formation of internal H-bond of 2.184 Å between the free axial C-H and a nearby -NO$_2$ group oxygen, specifically between O14 and H19, which also happens to be the shortest H-bond in IIIrec8. In Vrec1, an average shift of -32 cm^{-1} is registered for the C-H stretch in C-H$\cdots$O and -56 cm^{-1} shift for that in C-H$\cdots$Al interactions. The IBSIW values for these interactions show that the C-H$\cdots$O interactions are stronger, indicating that the shift of -56 cm^{-1} is not solely due to the C-H$\cdots$Al interactions. A cross-talk happens when O$_{corner}$ atoms of the Al$_3$O$_3^-$ (*rec*) are involved in H-bonding but not when O$_{center}$ atoms are involved.

New low frequency vibrations of the intact RDX motion against the $Al_3O_3^-$ part are present in the 80-130 cm^{-1} range in RDX$\cdots$Al$_3$O$_3^-$ (*kite*) and in the 60-100 cm^{-1} range in RDX$\cdots$Al$_3$O$_3^-$ (*rec*). The Al_{tail}-O(NO) interactions are reflected by new vibrations among the RDX$\cdots$Al$_3$O$_3^-$ (*kite*) between 50-80 cm^{-1}.

Current work indicates that C-H$\cdots$Al interactions as well as C-H$\cdots$O interactions will weaken C-H vibrations while perturbing the aluminum surface vibrations. Whether all the small shifts and low frequencies are detectable, distinct and useful depends on the resolution and the mode of the IR detection, its wavelength range, whether the measurement is conducted under vacuum or not, the laser polarization if used, and ultimately, whether the complexes covered here live long enough for detection.

Conclusions:

Weak interactions between five RDX isomers and two $Al_3O_3^-$ isomers are identified and corroborated by different analyses (NCI, IGMH, QTAIM, IQA) of the electron density from the DFT method (PBE0) using different basis sets (Def2-TZVPP, TZ2P) after optimization. A partial charge transfer from $Al_3O_3^-$ to RDX via the C-H$\cdots$O (1.851-2.481Å) and the C-H$\cdots$Al (2.836-2.871Å) interactions and back-transfer via the (ON)O$\cdots$Al interactions is quantified by different charge analyses (Hirshfeld, Mulliken, Hirshfeld-I, NPA) of the PBE0-D3/Def2TZVPP density and visualized by the EDA-NOCV analysis of the PBE0/TZ2P density. Hirshfeld analysis predicts 6-25% transfer of the -1 charge to RDX while Hirshfeld-I, NPA, and Mulliken predict 7-22%, 2-7%, and 7-13% transfer, respectively. The most dominant orbital interactions are the O(2p)-to-C-H(σ^*) type seen in H-bonds and Al(3p)-to-C-H(σ^*) type non-conventional H-bonds and $Al_3O_3^-$ (HOMO)-RDX (LUMO+3/LUMO+1) type of interactions. While RDX is excited by receiving electrons from $Al_3O_3^-$ it excites the $Al_3O_3^-$ back, resulting in a relocation of electrons which interestingly stabilizes the whole complex. The excitation of the $Al_3O_3^-$ is probable via the (ON)O$\cdots$Al interactions where the Al atoms have single or double coordination. This result shows that as RDX approaches the aluminum oxide defect, both species' excited states have to be incorporated into simulations.

Complexation weakens the bonds in the RDX heterocyclic ring and the N-O bonds while the N-N bonds become stronger. No mediation by H_2O, explicitly or implicitly, was necessary for

complex formation. The binding energies are in the -10- -31 kcal/mol range. The (RHF IP-EOM-DLPNO-CCSD) vertical detachment energies increase by 0.3-1.3 eV upon complexation, indicating that such defect sites hold onto electrons upon binding to RDX. Complex formation enriches the terahertz region of the IR spectra. The C-H stretch frequencies in 3000-3300 cm^{-1} region decrease by 10-350 cm^{-1}. Complexation and relaxation cause shifts in frequencies in the 0-1300 cm^{-1} region where the $Al_3O_3^-$ frequencies are located. Proximity to and interactions with -NO_2 groups excite out-of-plane vibrations. Complexation is found to generally augment the resultant dipole moment from 2.7 ($Al_3O_3^-$ (*rec*)) and 8.6 ($Al_3O_3^-$ (*kite*)) Debye to 2.9-16.0 Debye, signalling concrete effects on the workfunction of the aluminum oxide surfaces upon binding.

References:

1. Y. Yang et al., Journal of Applied Physics 95, 2004, 3667-3676; doi: 10.1063/1.1652250.

2. S. Wang et al., Chem. Phys. Lett. 368 (2003) 189–194. doi: 10.1016/S0009-2614(02)01846-8.

3. J. Stals, *Trans. Faraday Soc.* **1971**, *67*, 1768-1775; doi:10.1039/TF9716701768

4. J. N. Bradley et al., *J. Chem. Soc. Faraday Trans. 1* **1977**, *73*, 1789-1795; doi:10.1039/F19777301789.

5. M. Farber, *Mass Spectrom. Rev.* **1992**, *11*, 137-152 ; doi:10.1002/mas.1280110205.

6. S. M. Hankin et al., *Rapid Commun. Mass Spectrom.* **2002**, *16*, 111-116; doi:10.1002/rcm.553

7. R. G. Gillis et al.*, Org. Mass Spectrom.* **1974**, *9*, 359-364; doi:10.1002/oms.1210090317

8. J. Yinon et al., *Org. Mass Spectrom.* **1982**, *17*, 321-326; doi:10.1002/oms.1210170707

9. J. Yinon, *Org. Mass Spectrom.* **1987**, *22*, 501-505; doi:10.1002/oms.1210220805

10. X. Zhao et al. , *J. Chem. Phys.* **1988**, *88*, 801-810; doi:10.1063/1.454158

11. A. P. Snyder et al., *Org. Mass Spectrom.* **1989**, *24*, 15-21; doi:10.1002/oms.1210240104

12. M. Choi et al., *J. Phys. Chem.* **1995**, *99*, 15785-15789; doi:10.1021/j100043a016

13. J. Cabalo and R. Sausa, *Appl. Spectrosc.* **2003**, *57*, 1196-1199; doi:10.1366/00037020360696099

14. S. Maharrey and R. Behrens, *J. Phys. Chem. A* **2005**, *109*, 49, 11236-11249; doi:10.1021/jp054188q

15. Y. Q. Guo et al., *J. Chem. Phys.* **2005**, *122*, 244310; doi:10.1063/1.1929741

16. M. Greenfield et al., *Chem. Phys. Lett.* **2006**, *430*, 277-281; doi:10.1016/j.cplett.2006.09.025

17. P. Politzer and M. Yuguang, *Int. J. Quantum Chem.* **2004**, *100*, 733-739; doi:10.1002/qua.20237

18. S. Okovytyy et al., *J. Phys. Chem. A* **2005**, *109*, 2964-2970; doi:10.1021/jp045292v

19. D. Chakraborty et al., *J. Phys. Chem. A* **2001**, *105*, 1302-1314; doi:10.1021/jp0026181

20. T. B. Brill et al., *J. Propul. Power* **2002**, *18*, 824-834; doi:10.2514/2.6006

21. J.L. Lyman et al., *Combust. Flame* **2002**, *130*, 185–203; doi:10.1016/S0010-2180(02)00364-4

22. J.P. Lewis, *Chem. Phys. Lett.* **2003**, *371*, 588–593; doi:10.1016/S0009-2614(03)00309-9

23. D. Tsiaousis et al., *Chem. Phys.* **2004**, *305*, 317–323; doi:10.1016/j.chemphys.2004.07.013

24. B.M. Rice and E.F.C. Byrd, *J. Mater. Res.* **2006**, *21*, 2444-2452; doi:10.1557/jmr.2006.0329

25. E.F.C. Byrd et al. *J. Phys. Chem. B* **2004**, *108*, 13100-13106; doi:10.1021/jp0486797

26. J.D. White et al., *Appl. Optics* **2011**, *50*, 74-81. (Unpublished data) ; doi:10.1364/AO.50.000074.

27. R. B. Clarkson et al., *Molecular Engineering* 4 (1-3) 89-117, 1994; doi:10.1007/BF01004051.

28. Medvedev et al., *Phys. Chem. Chem. Phys.* 14 (8) 2587-2598, 2012; doi:10.1039/C2CP20863F.

29. G. Paglia et al., *Chem. Mater.* 2006, 18, 14, 3242-3248; doi:10.1021/cm060277j.

30. F. A. Akin and C. C. Jarrold, *J. Chem. Phys.* 118, 5841 (2003); doi: 10.1063/1.1553466.

31. F. A. Akin and C. C. Jarrold, *J. Chem. Phys.* 120, 8698-8706 (2004); doi: 10.1063/1.1687322.

32. F. J. Tenorio et al., *J. Chem. Phys.* 120, 7955-7962, (2004); doi: 10.1063/1.1689648.

33. A. Guevara-Garcia et al., *J. Chem. Phys.* 122, 214309 (2005); doi: 10.1063/1.1926279.

34. R. B. Wyrwas et al., *J. Chem. Phys.* 124, 201101 (2006); doi: 10.1063/1.2206583.

35. U. Das et al., *J. Chem. Phys.* 124, 021101, (2006); doi: 10.1063/1.2150813.

36. A. Guevara-Garcia et al., *J. Chem. Phys.* 126, 024309 (2007); doi: 10.1063/1.2409293.

37. U. Das et al., *J. Chem. Phys.* 127, 15, 154310 (2007); doi: 10.1063/1.2790012.

38. F. A. Akin and G. Kiyak, *Struct. Chem.* 30, 201-211 (2019); doi: 10.1007/s11224-018-1191-4.

39. Cheng et al., *Molecular Physics* 114 (12), 1931-1938, 2016; doi: 10.1080/00268976.2016.1169326.

40. S.K. Lee at al., *Phys. Rev. Lett.* 103, 095501 (2009); doi: 10.1103/PhysRevLett.103.095501.

41. S. Shi et al., *Advances in condensed matter physics* 2018 7598978 2018; doi:10.1155/2018/7598978.

42. T.V. Perevalov et al., *Eur. Phys. J. Appl. Phys.* 52, 30501 (2010); doi: 10.1051/epjap/2010159.

43. Århammar et al., *PNAS* 108, 6355-6360 (2011); doi: 10.1073/pnas.1019698108.

44. S. Canulescu et al., *Appl. Phys. Lett.* 104, 121910 (2014); doi: 10.1063/1.4866901.

45. Choi et al., *J. Appl. Phys.* 113 044501 (2013) doi: 10.1063/1.4784114.

46. E. Schiliro et al., *AIP Advances* 10, 125017 (2020) doi:10.1063/5.0023735.

47. H. Wu et al., *J. Chem. Phys.* 109, 449-458 (1998); doi: 10.1063/1.476583.

48. T. K. Ghanty and E. R. Davidson, J. *Phys. Chem. A* 1999, 103, 45, 8985-8993; doi: 10.1021/jp9925839.

49. F. A. Akin and C. C. Jarrold, *J. Chem. Phys.* 118, 1773 (2003); doi: 10.1063/1.1529176.

50. J. A. DeVine et al., *Faraday Discuss.* 2019, 217, 235-255; doi: 10.1039/C8FD00165K**.**

51. N. J. Harris and K. Lammertsma, *J. Am. Chem. Soc.* **1997**, *119*, 6583-6589. doi:10.1021/ja970392i.

52. C.S. Choi and E. Prince, *Acta Cryst.* B28, 2857 (1972); doi:10.1107/S0567740872007046.

53. D. I A. Millar et al., *Chem. Commun.* (2009), 34, 562; doi:10.1039/B817966B.

54. A. J. Davidson, et al., *CrystEngComm* (2008), 10, 162. ; doi:10.1039/B715677B.

55. C. Adamo, V. Barone, *J. Chem. Phys.* 110, 6158-6170 (1999); doi: 10.1063/1.478522.

56. A. Schaefer et al., *J. Chem. Phys.* 97, 2571-2577 (1992); doi: 10.1063/1.478522.

57. A. Schaefer et al., *J. Chem. Phys.* 100, 5829-5835 (1994); doi: 10.1063/1.467146.

58. S. Grimme et al. *J. Chem. Phys.* 132, 154104 (2010); doi: 10.1063/1.3382344.

59. S.F. Boys and F. Bernardi, Mol. Phys. 19, 553-566 (1986); doi: 10.1080/00268977000101561.

60. F. Weigend and R. Ahlrichs, *Phys. Chem. Chem. Phys.* 7 3297-3305, 2005; doi:10.1039/B508541A.

61. F. L. Hirshfeld, *Theoret. Chim. Acta.* 44, 129-138 (1977); doi: 10.1007/BF00549096.

62. R. S. Mulliken, *J. Chem. Phys.* 23, 1833-1846 (1955); doi: 10.1063/1.1740588.

63. P. Bultnick et al., *J. Chem. Phys.* 126, 144111 (2007); doi: 10.1063/1.2715563.

64. T. Lu and F. Chen, *J. Comput. Chem.* 33, 580-592 (2011); doi: 10.1002/jcc.22885.

65. NBO 7.0, E. D. Glendening et al., Theoretical Chemistry Institute, Madison (2018).

66. F. Neese, *Comput. Mol. Sci.* 2. 73-78, 2012; doi: 10.1002/wcms.81.

67. F. Neese, *Comput. Mol. Sci.* 8. e1327, 2017; doi: 10.1002/wcms.1327.

68. E.R. Johnson et al., *J. Am. Soc. Chem.* 132, 6498-6506 (2010); doi: 10.1021/ja100936w

69. T. Lu and Q. Chen, Theoretical and Comput. Chem. ; doi: 10.26434/chemrxiv-2021-628vh-v2

70. G. te Velde et al., Chemistry with ADF, *J. Comput. Chem.* 22, 931-967 (2001); doi: 10.1002/jcc.1056.

71. ADF 2023.1, SCM, Theoretical Chemistry, Vrije Universiteit, Amsterdam, The Netherlands, http://www.scm.com.

72. F. M. Bickelhaupt and E. J. Baerends In: Rev. Comput. Chem.; K. B. Lipkowitz and D. B. Boyd, Eds.; Wiley, NY, 2000, Vol. 15, p.1-86.

73. T. Ziegler and A. Rauk, *Inorg. Chem.* 18, 1558-1565 (1979); doi: 10.1021/ic50196a034

74. T. Ziegler and A. Rauk, *Inorg. Chem.* 18, 1755-1759 (1979); doi: 10.1021/ic50197a006

75. M. Mitoraj et al., *J. Chem. Theory Comput.* 2009, 5, 4, 962-975 (2009); doi:10.1021/ct800503d.

76. J.I. Rodriguez et al., *Chem. Phys. Lett.* 472, 149-152 (2009); doi: 10.1016/j.cplett.2009.02.081

77. J.I. Rodriguez, *J. Comput. Chem.* 34, 681-686 (2013); doi: .1002/jcc.23180.

78. F. A. Akin, *Molecular Physics* 114, 3556-3566 (2016); doi:10.1080/00268976.2016.1246759.

79. F. A. Akin, *Molecular Physics* 114, 3277-3293 (2016); doi:10.1080/00268976.2016.1229059.

80. Acikgoz et al., *Phys. Chem. Chem. Phys.* 21, 15080-15088, (2019); doi:10.1039/C9CP03105G.

81. Ma et al., *APL Mater.* 8, 07110 (2020); doi:10.1063/1.5143325.

82. Lee et al., *Acc. Chem. Res.* 48, 3007-3015 (2015); doi: 10.1021/acs.accounts.5b00307.

83. D. M. Alloway et al., *J. Phys. Chem. B* 107, 11690-11699 (2003); doi: 10.1021/jp034665+.

84. J. Kozelka in S. Scheiner (Ed.), Noncovalent Forces, Challenges and Advances in Computational Chemistry and Physics 19, doi:10.1007/978-3-319-14163-3_6.

85. He et al., *Chemistry-A European Journal* 17, 3449-3457 (2011); doi: 10.1002/chem.201002409.

86. Shi et al., *Sci. Rep.* 6 30123 (2016) doi:10.1038/srep30123.

87. Wischert et al., *J. Am. Chem. Soc.* 134, 14430-14449 (2012): doi: 10.1021/ja3042383.

88. Vasenin et al., *Doklady Physical Chemistry* 461 part 2, (2015); doi: 10.1134/S0012501615040016.